ISPRS Journal of Photogrammetry and Remote Sensing 134 (2017) 43–58

Contents lists available at ScienceDirect

ISPRS Journal of Photogrammetry and Remote Sensing

journal homepage: www.elsevier.com/locate/isprsjprs

# Unmanned Aerial System (UAS)-based phenotyping of soybean using multi-sensor data fusion and extreme learning machine

Maitiniyazi Maimaitijiang [a,b], Abduwasit Ghulam [a,b,*], Paheding Sidike [a,b], Sean Hartling [a,b], Matthew Maimaitiyiming [a,b], Kyle Peterson [a,b], Ethan Shavers [a,b], Jack Fishman [b], Jim Peterson [c], Suhas Kadam [e], Joel Burken [d], Felix Fritschi [e]

[a] Center for Sustainability, Saint Louis University, Des Peres Hall, Room 203, 3694 West Pine Mall, Saint Louis, MO, 63108, USA
[b] Department of Earth and Atmospheric Sciences, Saint Louis University, 3642 Lindell Blvd, Saint Louis, MO, 63108, USA
[c] Department of Polytechnic Studies, Southeast Missouri State University, One University Plaza, Cape Girardeau, MO 63701, USA
[d] Department of Civil, Architectural and Environmental Engineering, Missouri University of Science and Technology, 1401 N Pine St., Rolla, MO 65409, USA
[e] Division of Plant Sciences, University of Missouri, Columbia, MO 65211, USA

ARTICLE INFO

*Article history:*
Received 17 April 2017
Received in revised form 18 August 2017
Accepted 10 October 2017

*Keywords:*
Remote sensing
Unmanned Aerial System (UAS)
Phenotyping
Data Fusion
Extreme Learning Machine (ELM)
Extreme Learning Machine based Regression (ELR)

ABSTRACT

Estimating crop biophysical and biochemical parameters with high accuracy at low-cost is imperative for high-throughput phenotyping in precision agriculture. Although fusion of data from multiple sensors is a common application in remote sensing, less is known on the contribution of low-cost RGB, multispectral and thermal sensors to rapid crop phenotyping. This is due to the fact that (1) simultaneous collection of multi-sensor data using satellites are rare and (2) multi-sensor data collected during a single flight have not been accessible until recent developments in Unmanned Aerial Systems (UASs) and UAS-friendly sensors that allow efficient information fusion. The objective of this study was to evaluate the power of high spatial resolution RGB, multispectral and thermal data fusion to estimate soybean (*Glycine max*) biochemical parameters including chlorophyll content and nitrogen concentration, and biophysical parameters including Leaf Area Index (LAI), above ground fresh and dry biomass. Multiple low-cost sensors integrated on UASs were used to collect RGB, multispectral, and thermal images throughout the growing season at a site established near Columbia, Missouri, USA. From these images, vegetation indices were extracted, a Crop Surface Model (CSM) was advanced, and a model to extract the vegetation fraction was developed. Then, spectral indices/features were combined to model and predict crop biophysical and biochemical parameters using Partial Least Squares Regression (PLSR), Support Vector Regression (SVR), and Extreme Learning Machine based Regression (ELR) techniques. Results showed that: (1) For biochemical variable estimation, multispectral and thermal data fusion provided the best estimate for nitrogen concentration and chlorophyll (Chl) *a* content (RMSE of 9.9% and 17.1%, respectively) and RGB color information based indices and multispectral data fusion exhibited the largest RMSE 22.6%; the highest accuracy for Chl *a* + b content estimation was obtained by fusion of information from all three sensors with an RMSE of 11.6%. (2) Among the plant biophysical variables, LAI was best predicted by RGB and thermal data fusion while multispectral and thermal data fusion was found to be best for biomass estimation. (3) For estimation of the above mentioned plant traits of soybean from multi-sensor data fusion, ELR yields promising results compared to PLSR and SVR in this study. This research indicates that fusion of low-cost multiple sensor data within a machine learning framework can provide relatively accurate estimation of plant traits and provide valuable insight for high spatial precision in agriculture and plant stress assessment.



## 1. Introduction

Low-cost, high-throughput phenotyping is increasingly used to estimate plant traits including chlorophyll content, nitrogen (N) concentration, Leaf Area Index (LAI) and biomass (Gonzalez-Dugo

* Corresponding author at: Center for Sustainability, Saint Louis University, Des Peres Hall, Room 203, 3694 West Pine Mall, Saint Louis, MO, 63108, USA.
*E-mail address:* wasit.wulamu@slu.edu (A. Ghulam).

https://doi.org/10.1016/j.isprsjprs.2017.10.011
0924-2716/

et al., 2015; Saberioon et al., 2014; Salami et al., 2014; Singh et al., 2016; Thoele and Ehlert, 2010). Leaf Chlorophyll content generally is positively related with photosynthetic rate and plant productivity and provides valuable information about the physiological status of plants (Demmigadams and Adams, 1992; Gamon and Surfus, 1999). As such, it is a trait of interest for analyzing vegetation stress, nutrient cycling, growth stages, yield and diseases (Gitelson et al., 2006; Martinelli et al., 2015; Peng et al., 2011; Verrelst et al., 2012a). Leaf N concentration is a reflection of soil N availability, and in the absence of fertilization, N availability often limits plant growth, biomass production, and seed yield (Fichtner and Schulze, 1992; Gastal and Lemaire, 2002; Masclaux-Daubresse et al., 2010; Prasertsak and Fukai, 1997). Biophysical traits such as LAI and biomass are a reflection of growing conditions and management practices, and commonly are positively associated with yield (Liu et al., 2010; Serrano et al., 2000; Wang et al., 2017b). High-throughput and increased spatial precision in assessing these traits can aid in evaluating different genotypes throughout the growth season in field evaluations.

Traditionally, chlorophyll content and N status of leaf samples have been determined using extract-based, and digestion- or combustion-based approaches in the laboratory, whereas LAI and biomass measurements have been mainly based on destructive measurements which are accurate but relatively time and resource intensive (Lichtenthaler, 1987; Mistele and Schmidhalter, 2008; Mora et al., 2016; Richardson et al., 2002). More recently, alternative, non-destructive approaches including hand-held instruments based on optical methods have become more popular for the determination of chlorophyll content, N concentration (*i.e.*, SPAD-502, Dualex 4 Scientific, and CCM-200 chlorophyll meter) and LAI (*i.e.*, LI-Cor 2000/2200, AccuPAR LP-80) (Breda, 2003; Cartelat et al., 2005; Cerovic et al., 2012; Munoz-Huerta et al., 2013).

In contrast to traditional analyses, remote sensing provides a rapid estimation of plant biochemical and biophysical parameters for large areas in field-scale trials (Furbank and Tester, 2011; Li et al., 2014). Recent developments in Unmanned Aerial Systems (UASs) and sensors have resulted in low-cost and flexible solutions that can provide images at high spatial, temporal, and spectral resolution. Equipped with multiple imaging sensors, autopilots, and GPS systems, UASs have become one of the most competitive remote sensing tools offering great possibilities for precision agriculture (Hunt et al., 2005; Primicerio et al., 2012; Schirrmann et al., 2016) and high-throughput phenotyping (Haghighattalab et al., 2016; Sankaran et al., 2015; Shi et al., 2016). In addition, UASs can complement ground-based robots by increasing throughput and frequency of non-destructive plant monitoring (Shi et al., 2016).

Based on the types of sensors mounted on UASs, different agronomic parameters and phenotypic traits have been reported in previous studies. First, steady color cameras that acquire true color (i.e., RGB) digital photographs in the Visible (VIS) Spectrum are some of the most commonly used sensors that are relatively cost-efficient and light-weight (Hunt et al., 2008). Color information from RGB images can be utilized to estimate leaf chlorophyll content and N concentration (Li et al., 2015; Schirrmann et al., 2016), LAI (Chianucci et al., 2016; Corcoles et al., 2013; Mathews and Jensen, 2013), plant height and biomass (Bendig et al., 2014; Schirrmann et al., 2016; Zarco-Tejada et al., 2014). Further, 3D geometry derived from RGB image allows Crop Surface Model (CSM) generation and plant height estimation (Bendig et al., 2014). Second, low-cost multispectral sensors in VIS and Near Infrared (NIR) spectral regions allow extraction of both physiological and geometric properties of vegetation (Houborg and Boegh, 2008) as well as accurate estimation of chlorophyll content, N concentration and yield for a variety of crops (Caturegli et al., 2016; Rey-Carames et al., 2015). Third, relatively expensive hyperspectral sensors with hundreds to thousands of contiguous spectral bands have been proven very effective for estimation of chlorophyll content (Uto et al., 2013), carotenoid content (Zarco-Tejada et al., 2013), N concentration, biomass (Honkavaara et al., 2013), plant height, LAI (Kalisperakis et al., 2015), and yield (Gonzalez-Dugo et al., 2015). In addition to passive optical sensors, Light Detection and Ranging (LiDAR), which is capable of providing three-dimensional information on canopy structure (Hofle, 2014), has been used to derive canopy height, fractional cover, and above ground biomass (Wang et al., 2017a). Fourth, thermal sensors provide plant canopy temperature, which has been used to detect water stress (Berni et al., 2009; Zarco-Tejada et al., 2012). It is worth noting that LiDAR-derived height information is critical for scaling leaf level traits to canopy (Gökkaya et al., 2015) and LiDAR-optical data fusion can overcome saturation problems inherent in optical remote sensing (Wallace, 2013).

Fusion of images collected from a UASs integrated with multiple sensors have become popular in recent years because data fusion improves plant trait estimation by combining advantages of rich spectral, spatial, structural and thermal information contained in diverse sensor systems. For instance, spectral and LiDAR structural data fusion was applied for biomass estimation (Marshall and Thenkabail, 2015; Tilly et al., 2015; Wang et al., 2016); spectral indices and plant height from CSM based on RGB imagery were combined for biomass estimation and crop yield (Bendig et al., 2014, 2015; Geipel et al., 2014; Li et al., 2016); and spectral information from a multispectral sensor and canopy temperature information from a thermal sensor was utilized for chlorophyll concentration estimation (Elarab et al., 2015). It is evident from these studies that data fusion is able to improve estimations (Elarab et al., 2015; Reddersen et al., 2014; Tilly et al., 2015), potentially resolving saturation problems often observed with VIS-NIR sensor data, especially for higher density vegetation (Thenkabail et al., 2000; Tilly et al., 2015).

Thermal properties of plant leaves impact their photosynthetic ability, and consequently influences leaf nutrients status such as N and chlorophyll concentration (da Luz and Crowley, 2010; Salvucci and Crafts-Brandner, 2004; Sharkey, 2005). Thermal data has potential to elucidate the biophysical or biochemical characteristics of vegetation, complementing other remote sensing data to some extent (Ullah, 2013). Plant canopy temperature has been used to assess plant transpiration for many years (Ehrler, 1973; Sepulcre-Cantó et al., 2006; Virlet et al., 2014; Zarco-Tejada et al., 2012); however, compared with optical multispectral and hyperspectral remote sensing, only few studies have examined the application of thermal remote sensing for chlorophyll concentration (Elarab et al., 2015), N concentration, biomass, yield (Du et al., 2011; Gonzalez-Dugo et al., 2015; Guo et al., 2016; Tattaris et al., 2016), and LAI estimation (Neinavaz et al., 2016). Additionally, the potential integration of thermal remote sensing in the context of data fusion for UAS aerial plant phenotyping is little understood.

A number of statistical methods exist for modelling plant traits based on UAS imagery data, including Multiple Linear Regression (MLR), Partial Least Squares Regression (PLSR) (Araus and Cairns, 2014; Rischbeck et al., 2016), and Machine Learning (ML) algorithms (Cipollini et al., 2001; Elarab et al., 2015; Hassan-Esfahani et al., 2015; Singh et al., 2016; Verrelst et al., 2012b). Nevertheless, it still remains to be established if ML methods are more powerful for parameter estimation in remote sensing applications (Verrelst et al., 2012b). Many ML methods (e.g., Supper Vector Machine (SVM)) (Cortes and Vapnik, 1995; Moser and Serpico, 2009) contain large computational complexity, such as tuning learning parameters that may impact the robustness of the model. Moreover, processing an enormous volume of remote sensing data requires considerable training time for a ML algorithm that also necessitates considerable computational power. Among ML algorithms, Extreme Learning Machine (ELM) (Huang et al., 2006) is an efficient and rapid learning algorithm for regression and classification analysis (Huang et al., 2012) that outperformed many other ML methods for many practical applications (Alom et al., 2016; Chen et al., 2016; Moreno et al., 2014; Savojardo et al., 2013; Sidike et al., 2017). Two distinct properties of ELM include: (1) hidden node parameters are randomly generated instead of iterative tuning, thus enhancing computational efficiency; (2) only a single parameter (i.e., the number of hidden nodes) is required for tuning in the basic ELM. Several studies (Huang et al., 2006; Zhang et al., 2016) have shown that ELM provides similar or even better generalization performance than SVMs and Back-Propagation algorithms (Williams and Hinton, 1986).

The primary objective of this study was to estimate soybean chlorophyll *a* (Chl *a*), chlorophyll *b* (Chl *b*), and chlorophyll *a* + *b* (Chl *a* + *b*) contents, N concentration, above ground fresh and dry biomass, and LAI by combing low-cost RGB, multispectral, and thermal data acquired by UASs using both empirical statistical PLSR and selected ML methods. To that end, the contribution and potential of data from each individual sensor (RGB, multispectral, and thermal) to phenotype estimation within the framework of data fusion along with ML were evaluated.

## 2. Materials

### 2.1. Field site and crop management

To evaluate the potential of low-cost UAS sensors on plat phenotype estimates, a comprehensive field campaign aimed at collecting UAS-based RGB, multispectral, and thermal images, as well as ground-truth phenotype metrics was conducted at an experimental soybean field located at the Bradford Research Center near Columbia, Missouri (38.8N, 92.2W). Soybean was grown on a Mexico silt loam (fine, smectitic, mesic Vertic Epiaqualf) soil with a pH of 6.5. After tillage, soybean cultivars ‘Pana’, ‘Dwight’, and ‘AG3432’ were planted at 2.5-cm depth in rows 0.76 m apart to a density of 40 seed per $m^2$ on May 25, 2016. The field was laid out in four replications each with irrigated and rainfed main plots and Pana and Dwight as split-plots measuring 15 × 24 m or 9 × 24 m. To separate irrigated and rainfed plots, buffers were planted with AG3432 as illustrated in Fig. 1. No fertilizers were applied and weeds were controlled by application of the pre-emergence herbicide sulfentrazone at a rate of 0.3 kg ai $ha^{-1}$ and post-emergence herbicide sethoxydim at a rate of 2.6 kg $ha^{-1}$. Due to abundant rainfall during most of the season, only one irrigation of 2.5 cm was applied using an overhead linear move lateral system on June 25, 2016. Because of unexpected rainfall within hours of irrigation and continued abundant precipitation, no differences between rainfed and irrigated treatments materialized. Soybean harvest was conducted on October 15, 2016 with a small-plot research combine. Temperatures as measured by the on-farm weather station during the growing season averaged 16.85 °C in May, 24.68 °C in June, 24.64 °C in July, 23.61 °C in August, 20.96 °C in September, and 16.02 °C in October. Monthly precipitation recorded by the same weather station was 81 mm in May, 29 mm in June, 274 mm in July, 149 mm in August, 142 mm in September, and 25 mm in October.

### 2.2. Data acquisition

#### 2.2.1. Ground data

For precise ground truthing of UAS data, sampling locations within each plot were marked with wood sticks for the duration of the experiment (Fig. 1). Seventy days after the plantation (on August 4, 2016), biophysical and biochemical measurements were taken simultaneously during the UAS flights. The LAI was measured nondestructively using LAI-2200C Plant Canopy Analyzer (LI-COR Inc., Lincoln, NE, USA) which allows users to operate under full sun condition without further requirements for sun angle. Measurements were conducted along a diagonal transect between the row marked with the stakes and a neighboring row using the 45° view restrictor to hide the user from the sensor Field of View (FOV). Between two above canopy reading at the beginning and end of the rows, five below canopy readings were taken along the transect at even spacing by placing the sensor on the ground to assure maximum coverage of the soybean canopy was in the sensor FOV.

Non-destructive measurement of biochemical pigments were obtained on the uppermost, fully expanded, mature trifoliate leaf at each sampling point using a DUALEX 4 Scientific (Force-A, Orsay, France) hand-held sensor that calculates leaf chlorophyll index (Chl), flavonol index (Flv) and a Nitrogen Balance Index (NBI) by chlorophyll fluorescence screening and differential transmittance methods (Bilger et al., 2001; Cerovic et al., 2012; Goulas et al., 2004). These measurements were taken from a plant within the sampling location. Leaf chlorophyll index was calculated using $(T_{850} - T_{710})/T_{710}$, where T is the leaf transmittance, and the subscripts are wavelengths in nanometers (nm). NBI was determined using $[(Chl_{AD} + Chl_{AB})/2]/(Flv_{AD} + Flv_{AB})$, where the Flv was expressed as $\log(FRF_R/FRF_{UV})$ using the far-red Chl fluorescence (FRF) emission excited by Red (R) or Ultra-Violate (UV) light. The subscripts AD and AB stand for adaxial and abaxial sides of the leaf, respectively. In this study, NBI was used as measure of the plant N concentration.

To get a better estimate of leaf chlorophyll contents, 1.168 $cm^2$ circular samples were excised from the same leaves used for DUALEX 4 measurements and circular samples were placed in a glass vial containing 5 mL of 95% ethanol. Following 24 h of incubation at room temperature, the vials were shaken and 200 μL of supernatant was transferred to 96-well plates for absorbance measurements at 664.1 and 648.6 nm using a Scanning Monochromatic Spectrophometer (BioTek PowerWave X 340 Microplate Reader, BioTek U.S. VT, USA). The contents of chlorophyll *a* and *b* were calculated using the following equations (Lichtenthaler and Buschmann, 2001) and expressed on a leaf area basis (μg $cm^{-2}$):

$$\text{Chl } a \text{ (chlorophyll } a) = 13.36_{664.1} - 5.19_{648.6} \tag{1}$$

$$\text{Chl } b \text{ (chlorophyll } b) = 27.43_{648.6} - 8.12_{664.} \tag{2}$$

$$\text{Chl } a + b = \text{Chl } a + \text{Chl } b \tag{3}$$

where *A* is the absorbance of the extract solution, and the numeric subscripts are wavelengths in nanometers (nm).

Plant height was measured for five sampling locations (five plants) in a row and averaged for further analysis. On the same day, above ground plant biomass samples were collected by cutting the stems approximately 2 cm above the soil over 1 m row length from each of two rows (1.52 $m^2$) (Fig. 1). After fresh weight determination, plants were oven-dried at 60 °C until weights stabilized, and dry samples were weighed to obtain above ground dry biomass. The descriptive statistics of measured biochemical and biophysical plant traits shows in Table 1.

#### 2.2.2. UAS imagery

On August 4, 2016, ground and UAS field campaign was conducted from 10:30AM through 3:00 PM local time. RGB color imagery was acquired using a Sony Alpha ILCE-7R RGB camera mounted on a DJI S900 hexacopter (Fig. 2a). The DJI S900 frame weighs 3.3 kg with a maximum takeoff weight of 8.2 kg. Under optimal weather conditions, the S900 vehicle is capable of a maximum flight time of 18 min at a takeoff weight of 6.8 kg operating

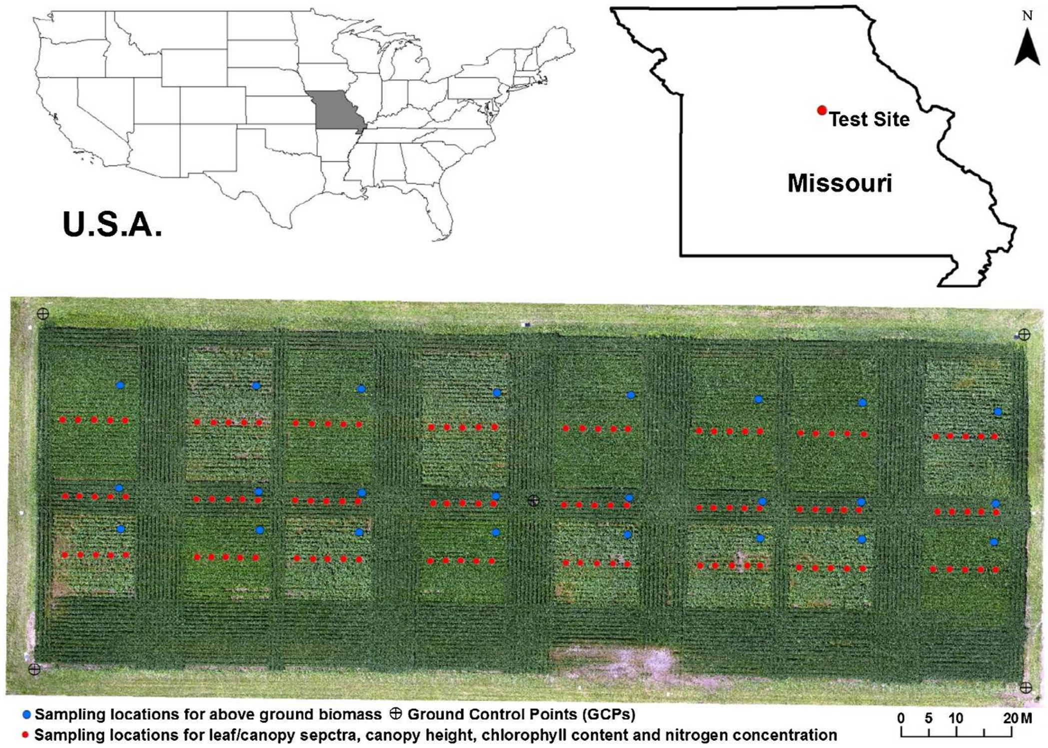


**Fig. 1.** Test site location. Red dots are sampling locations for leaf/canopy spectra, canopy height, chlorophyll content, and nitrogen concentration, blue dots represent above ground biomass sampling locations, and stars are locations of Real Time Kinematic (RTK) GPS survey Ground Control Point (GCP). (For interpretation of the references to color in this figure legend, the reader is referred to the web version of this article.)

**Table 1**
Descriptive statistics of biochemical and biophysical parameters.

| Parameters | Mean | Max. | Min. | SD | CV (%) |
|---|---|---|---|---|---|
| Chl *a* (μg cm$^{-2}$) | 37.69 | 46.86 | 23.39 | 5.25 | 13.99 |
| Chl *b* (μg cm$^{-2}$) | 16.86 | 30.98 | 7.41 | 4.71 | 27.93 |
| Chl *a* + *b* (μg cm$^{-2}$) | 54.55 | 71.16 | 31.68 | 8.48 | 15.54 |
| N | 30.95 | 59.50 | 12.40 | 11.71 | 37.83 |
| LAI | 4.76 | 6.20 | 2.10 | 1.21 | 25.40 |
| FB (g m$^{-2}$) | 1533.58 | 2144.00 | 802.00 | 334.71 | 21.83 |
| DB (g m$^{-2}$) | 333.58 | 463.00 | 208.00 | 64.97 | 19.48 |

LAI: leaf area index; FB: fresh weight of biomass in grams per square meter; DB: dry weight of biomass in grams per square meter; N: nitrogen concentration which is represented by Nitrogen Balance Index (NBI); SD: standard deviation; CV: coefficient of variation.

on a 6S 12,000 mAh battery. The camera was mounted to the S900 frame on a Ronin 3-axis gimbal to stabilize image capture. Sony's Alpha ILCE-7R camera employs a 36.8 megapixel 35 mm full frame Exmor® CMOS sensor and images in this study were captured in 0.04 m pixel resolution.

Multispectral (MSI) and Thermal (TR) images were acquired using a Parrot Sequoia multispectral sensor and an ICI 8640 P-series thermal camera, respectively. The sensors were mounted on a DJI S1000 + octocopter frame (Fig. 2b). The DJI S1000 + frame weighs 4 kg with a max takeoff weight of 11 kg. Under optimal weather conditions, the S1000 is capable of a maximum flight time of 15 min as powered by a 6S 15,000 mAh battery at a takeoff weight of 9.5 kg. The Parrot Sequoia multispectral and accompanying sunshine radiance sensors were hard mounted to the frame while the ICI thermal camera was mounted on a custom designed two-axis gimbal (Fig. 3c). The gimbal mount was constructed from ABS plastic printed on an Afinia H800 3D printer and utilized two Lumenier brushless gimbal motors controlled by a BaseCam SimpleBGC gimbal controller. The Parrot Sequoia camera imaged with one 16 megapixel rolling shutter RGB camera at 4608 × 3456 pixel resolution and four 1.5 megapixel global-shutter single band cameras imaging at 1280 × 960 pixel resolution in the green (550 nm), red (660 nm), red-edge (735 nm) and near infrared (790 nm) spectral bands. The Parrot Sequoia sunshine sensor recorded the intensity of light emanating from the sun in the same four bands of light. The ICI 8640 P-series thermal camera imaged at a 640 × 512 pixel resolution in the 7–14 nm spectrum range and a temperature range of −40 °C to 500 °C.

All flight systems were equipped with a 3D Robotics Pixhawk autopilot controller enabling user-defined autonomous waypoint flight operations. Flight missions were planned utilizing Mission Planner, an open source full-featured ground station application for UAS autopilot systems. All missions were planned at a flight altitude of 30 m with an intended overlap of 90% and sidelap of 80% to ensure image redundancy for post-processing. Flight missions remained constant throughout the study period to ensure consistency in data collection. Ground truth measurements for georeferencing imagery were acquired at the center and the four corners of the field, using a Trimble R8 GNSS Rover (Fig. 2d) with access to the Missouri Statewide Real Time GNSS Network.

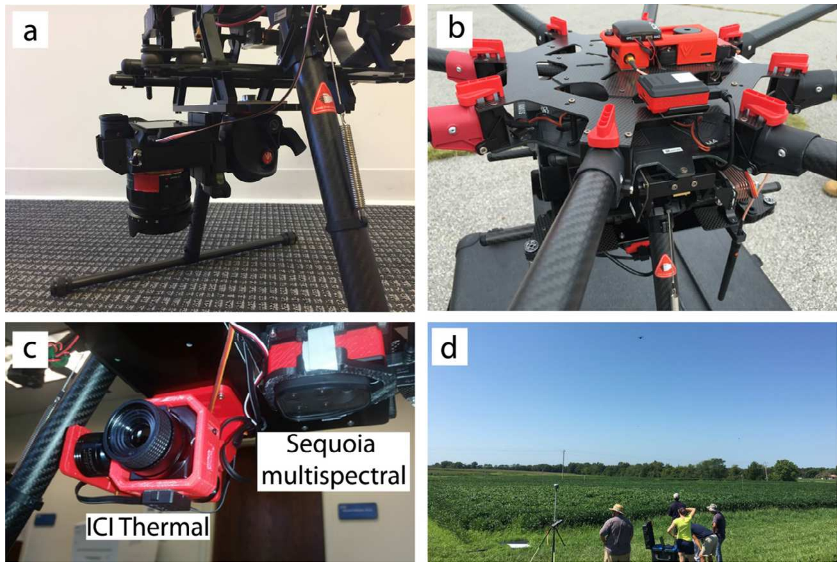


**Fig. 2.** UAS systems and integrated sensors. Sony Alpha ILCE-7R camera is mounted on a S900 hexacopter (a), Parrot Sequoia irradiance sensor on DJI S1000+ integrated with 3D Robotics Pixhawk autopilot controller (b), ICI thermal and Sequoia multispectral sensors on the bottom of DJI S1000+ UAS (c), and Trimble R8 GNSS Rover (d).

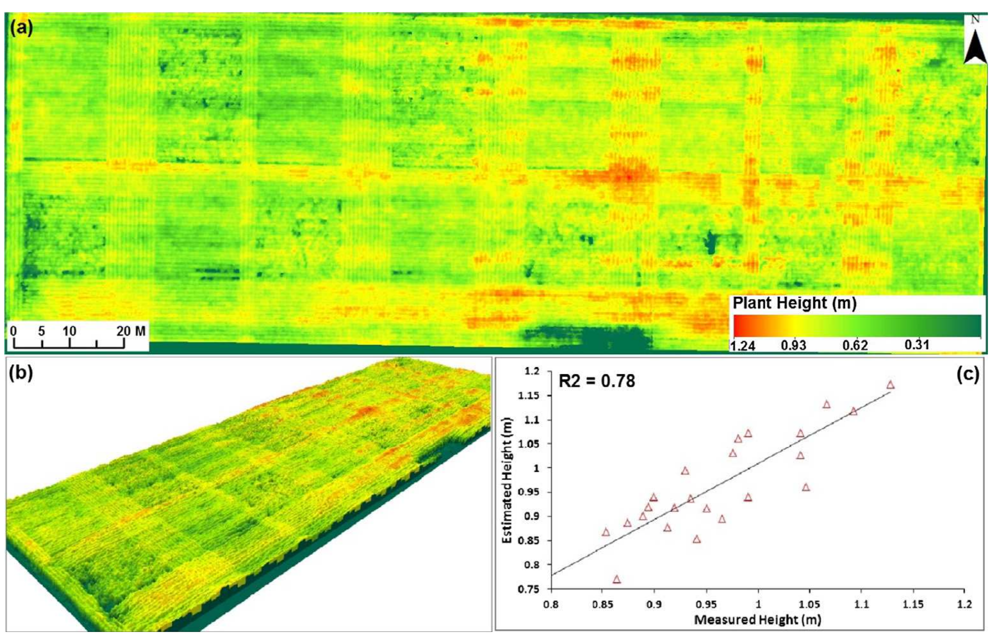


**Fig. 3.** Plant height estimation map showing entire field (a), 3D view of plant height distribution (b), and scatter plot of field measured and estimated plant height (c).

### 2.3. Image pre-processing

Images gathered by the Parrot Sequoia Multispectral sensor generated datasets for each flight that included Green, Red, Red-edge, and NIR reflectance. The Parrot Sequoia Multispectral sensor is a self-calibrating system that incorporates an integrated irradiance sensor. The irradiance sensor allows sunlight information to be logged and captured throughout the flight. Utilizing these irradiance values the system automatically calibrates all output images along with assigning geolocation information from the Parrot Sequoia's onboard GPS, IMU, and Magnetometer. Raw thermal infrared imagery gathered by the ICI 8640 P sensor generated a dataset of jpeg images containing Digital Number (DN) values that represent emitted radiant energy intensity. To access true temperature values from the imagery, the raw images were radiometrically calibrated using proprietary software from ICI and transformed into degrees Celsius utilizing factory calibration data and radiative transfer equations. These calibrated images were then saved in 32-bit Tagged Image Format File (TIFF) so that true temperature values can be retained. Once the corrected temperature values were generated, geolocation data was assigned to each image using information obtained from the UAS's flight log.

Radiometrically calibrated images were then mosaicked using the Pix4Dmapper software package (Pix4D SA, Lausanne, Switzerland). The Pix4Dmapper software is specifically designed to process UAS data and utilizes techniques rooted in both computer vision and photogrammetry to overcome the lack of precise sensor information such as GPS and IMU (Inertial Measurement Unit) information common in UAS data (Chao et al., 2010; Turner et al., 2012). To improve the accuracy of the final mosaics, camera information such as sensor dimensions, principal points, pixel size, and focal length, along with survey grade Ground Control Points (GCPs) were incorporated. Utilizing a combination of input data, the software searches and creates matching points by analyzing all images. A bundle block adjustment was then used to reconstruct the exact position and orientation of the sensor for every acquired image. From this reconstruction the matching points were verified and their resulting 3-D coordinates were calculated based on each image's GPS information. This 3-D point cloud was then interpolated to create a Triangulated Irregular Network (TIN) that was in turn used to form a Digital Surface Model (DSM). Finally, the resulting DSM was used to project each pixel and calculate the orthomosaic (Strecha et al., 2012). To finalize the data products, generated orthomosaics for Red, NIR, Red-edge, Green, and thermal bands were geo-referenced to NAD 1983 UTM Zone 15N creating a unified imagery dataset.

## 3. Methods

### 3.1. Feature extraction from imagery

#### 3.1.1. Vegetation index extraction

A set of vegetation indices was extracted from orthorectified RGB, MSI and TR images (Table 2). Average pixel values were calculated within 1 m (row length direction) by 1.52 m (two row widths) square buffer around each sampling point for each index to relate them to the phenotypic and agronomic measurements. Pearson correlation analysis, which is one of the widely used methods for indicating correlation between variables, is employed in our study. We first calculated Pearson correlation coefficients between vegetation indices and in-situ data, and then selected indices showed relatively strong and significant correlation for further modelling analysis (Rey-Carames et al., 2015; Rischbeck et al., 2016). However, Pearson correlation may not be a good indicator of the association between the spectral variables and the biophysical parameters when a machine learning method is applied to learn patterns in a multidimensional space. This is because it only assumes a linear relationship between variables, it is thus likely misinterprets relationship between the variables that are in non-linear form (Hauke and Kossowski, 2011). In addition to single band information, normalized indices were used because they are comparatively less sensitive to changes in illumination and viewing geometry (Galvao et al., 2013).

#### 3.1.2. Plant height estimation and calibration

Plant height extracted from RGB imagery is critical for biomass and yield estimation (Geipel et al., 2014; Tilly et al., 2015). 4 cm resolution DSMs (Digital Surface Models; also regarded as CSM) was derived using Pix4Dmapper's point cloud generation and 3D scene reconstruction tool, which is based on Structure from Motion (SfM) technique using Very High Resolution (VHR) RGB orthoimages (Rose et al., 2015; Su et al., 2016). In order to georeference the DSMs and increase the accuracy, 5 GCPs measured using differential GPS units were imported into Pix4D Mapper, and, prior to 3D scene generation, were manually placed on 5 corresponding images to project the remaining images automatically (Lucieer et al., 2014). A one meter resolution LiDAR-derived Digital Elevation Model from the USGS National Elevation Dataset (USGS, 2016) was registered to our DSM, and plant height was estimated as the difference between the DSM and DEM (Bendig et al., 2015; Geipel et al., 2014). The DSM and DEM subtraction based plant height was validated and calibrated based on comparison of plot level average plant height with the ruler-based field surveyed ground truth (Fig. 3).

#### 3.1.3. Vegetation fraction estimation

Vegetation Fraction (VF) is defined as the percentage of green vegetation area per ground surface area, which provides important crop density and structural (i.e., LAI) information (Schirrmann et al., 2016). We extracted vegetation area from ultra-high resolution RGB images using SVM based classifier. Consequently, sunlit and shaded soil was identified and excluded (Fig. 4) from further processing for biochemical traits Chl *a*, Chl *b*, Chl *a* + *b* and N concentration estimation. Vegetation fraction was then calculated by dividing pixels that were classified as vegetation in each plot by all pixels in that plot (Torres-Sanchez et al., 2014). The classification result was tested using randomly selected 1500 training samples with an overall accuracy of 99.59% and Kappa coefficient of 0.993.

### 3.2. Modelling methods

#### 3.2.1. Feature fusion and representation

Regression model in ML domain typically utilizes one or a set of discrete attributes or features that represent objects of interest, and then a linear or nonlinear relationship can be found stochastically between the input features and the observation. Generally, the extracted features from a single sensor may not provide rich or sufficient information to find that relationship, thus it is highly recommended to integrate features from multiple sensors into a united one to better represent the objects of interest. In this work, we propose to combine various features that are extracted from RGB, MSI, and TR images, and then verify the benefits of using information from various sensors to estimate phenotypic parameters. Table 3 shows detailed data information used in our experiments.

**Table 2**
List of Vegetation Indices extracted from visible, multispectral, and thermal images.

| Image | Index | Acronym | Equation | References |
|---|---|---|---|---|
| RGB | Red | R | R | / |
| | Green | G | G | / |
| | Blue | B | B | / |
| | Color intensity | INT | (R + G+B)/3 | Ahmad and Reid (1996) |
| | Kawashima index | IKAW | (R − B)/(R + B) | Kawashima and Nakatani (1998) |
| | Principal component analysis index | IPCA | 0.994\|R − B\| + 0.961\|G − B\| + 0.914\|G − R\| | Saberioon et al. (2014) |
| MSI | Green Band | Green | Green | / |
| | Red Band | Red | Red | / |
| | Red-edge Band | RE | RE | / |
| | Near-infrared Band | NIR | NIR | / |
| | Normalized difference vegetation index | NDVI | (NIR − R)/(NIR + R) | Rouse (1974) |
| | Green Normalized difference vegetation index | GNDVI | (NIR − G)/(NIR + G) | Gitelson et al. (1996) |
| | Normalized difference red edge | NDRE | (NIR − RE)/(NIR + RE) | Barnes et al. (2000) |
| TR | Canopy Temperature | Tc | Tc | / |

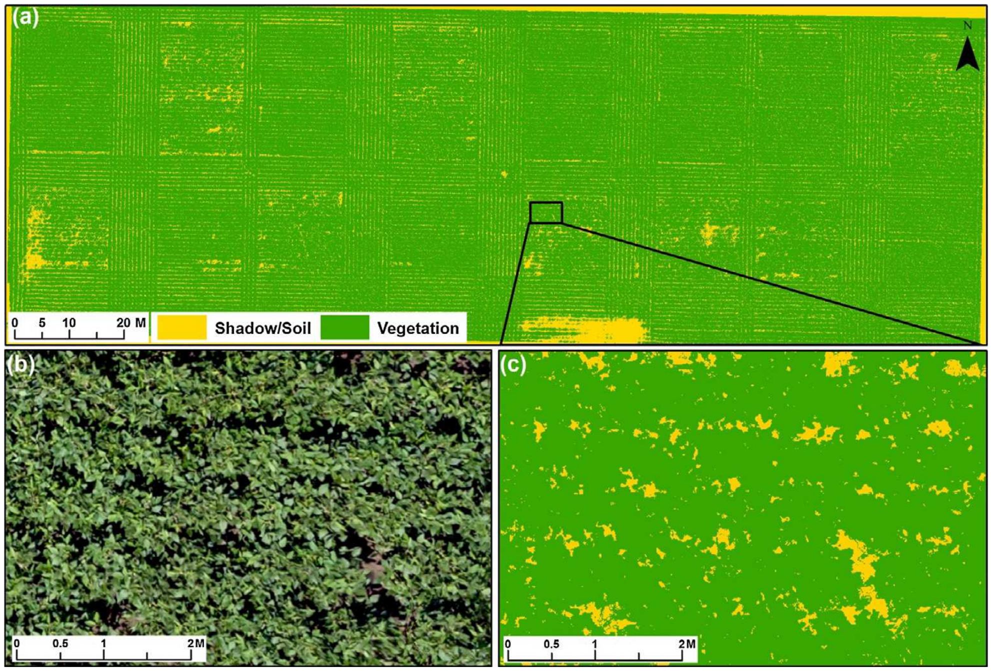


**Fig. 4.** Vegetation fraction and soil and shadow removal. (a) shows the entire field, (b) is a close-up RGB image, and (c) shows the corresponding vegetation and shadow/soil map of the close-up view.

**Table 3**
Image type with the corresponding futures. R, G, and B represent red, green, and blue bands of RGB sensor, respectively. INT is color intensity index, IKAW is Kawashima index, IPCA is principal component analysis index, PH is plant height, VF is vegetation fraction; Green, Red, RE and NIR represent green, red, red-edge and near-infrared bands of multispectral sensor, respectively. NDVI is normalized difference vegetation index, GNDVI is green normalized difference vegetation index, NDRE is normalized difference red-edge index; Tc is plant canopy temperature.

| Image Type | Information Type | Corresponding features |
|---|---|---|
| RGB | Color info. (DN)<br>Physical structure info. | R, G, B, INT, IKAW, IPCA<br>PH, VF |
| MSI | Spectral info. (Ref.) | Green, Red, RE, NIR, NDVI, GNDVI, NDRE |
| TR | Thermal info. (°C) | Tc |

Note: DN: Digital number; Ref.: Reflectance.

Considering potential contributions of various features for the prediction of bio-physicochemical parameters, the abovementioned features are combined and then fed into ELM based Regression (ELR). Consequently, each sampling point in the data set contains a set of variables, which are obtained by concatenating all the features from three different sensors, mathematically expressed as:

$$\boldsymbol{x}_i = [x_1, x_2, \ldots, x_d], \quad for\ i = 1, 2, \ldots, N \tag{4}$$

where $\boldsymbol{x}_i$ is input feature vector for each data sample,$d$ is the total number of extracted features, and $N$ is the total number of sampling points in the data set.

### 3.2.2. Feature learning and prediction using ELR

Extreme Learning Machine (ELM) can be used for classification and regression applications. We denote ELM based regression as ELR. The classic ELM is a Single-hidden Layer Feedforward Neural network (SLFN) that contains a single input layer, one hidden layer, and one output layer. In ELM, the weights of the hidden layer can be randomly generated without iterative optimization (Huang et al., 2006), leading to significantly less computational time to train the model. Previously, Moreno et al. (2014) showed that ELM provides excellent performance for soybean classification. Here, we utilize ELM for regression analysis, i.e., ELR model to predict plant phenotypes from UAS imagery. To the best of our knowledge, this is the first time that ELR has been implemented for predicting UAS imagery based plant phenotyping traits with clearly demonstrating the benefits of various data fusion. Fig. 5 shows the algorithmic flow using the extracted multiple data features implemented in this study.

To build the model, pairs of distinct samples $\{\boldsymbol{x}_i, y_i\}_{i=1}^{N}$ are selected from a given training set of $N$ input vectors $\boldsymbol{x}_i \in \mathbb{R}^d$ with the corresponding $N$ output values $\{y_i\}_{i=1}^{N}$. The goal of using ELM is to find a relationship between input $\boldsymbol{x}_i$ and the desired output $y_i$. To achieve this, the following cost function for $L$ hidden nodes is minimized as

$$\min \|y_i - \hat{y}_i\|_{i=1}^{N} = \min_{\beta} \sum_{i=1}^{N} \left( y_i - \sum_{j=1}^{L} \beta_j h_j(\boldsymbol{w}_j \cdot \boldsymbol{x}_i + b_j) \right)^2 \tag{5}$$

where $\hat{y}_i$ is the predicted output. The $j$th output weight vector, denoted as $\beta_j$ is the output weight links the $j$th hidden node and the output node. $\mathcal{R}(\boldsymbol{x}_i) = g(_j, b_j, \boldsymbol{x}_i)$ is the output of the $j$th hidden node with respect to the input $\boldsymbol{x}_i$, $g(\cdot)$ is a nonlinear piecewise continuous function (e.g., Sigmoid function), $_j \in \mathbb{R}^d$ is the weight vector connecting $j$th hidden node and the input nodes, and $b_j$ is the bias of the $j$th hidden node. Traditionally, in order to train a SLFN, hidden layer parameters$(_j, b_j)$ are optimized throughout gradient-descent or global search methods. In contrast, those parameters are randomly generated without iteratively tuning in ELM, and only the output weights $\beta_j (j = 1, 2, \ldots, L)$ are optimized using least-square error analysis. Consequently, ELM is capable of processing large amount of data with a faster learning speed. For $N$ number of training samples, a compact form can be written by as

$$\mathcal{H}\boldsymbol{\beta} = \boldsymbol{Y} \tag{6}$$

where $\boldsymbol{Y} = [y_1, y_2, \ldots, y_N]^{\boldsymbol{T}}$ is the desired output values, $\boldsymbol{H}$ refers to the hidden-layer output matrix, and $\boldsymbol{\beta} = [\beta_1, \beta_2, \ldots, \beta_L]^{\boldsymbol{T}}$ is the vector

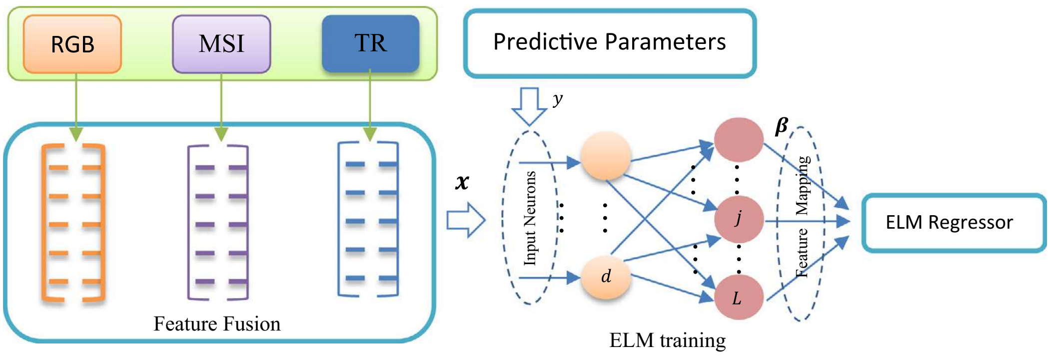


**Fig. 5.** Block diagram utilized for feature fusion based regression process.

of the output weights, which can be obtained by the minimal least square method (Huang et al., 2006; Rao and Mitra, 1971). Accordingly, the estimated value for the $i$th input is obtained by

$$\hat{y}_i = \mathcal{R}(\boldsymbol{x}_i)\mathcal{H}^{\boldsymbol{T}}\left(\frac{\boldsymbol{I}}{\rho} + \mathcal{H}\mathcal{H}^{\boldsymbol{T}}\right)^{-1}\boldsymbol{Y} \tag{7}$$

where $\rho$ a user-specified parameter and $I$ is an identity matrix. More details of ELM can be found in (Huang et al., 2006, 2012).

*3.2.3. Quantitative evaluation*

To quantitatively assess the performance of the proposed model for predicting biophysical and biochemical parameters, various popular elevation metrics, such as Root Mean Square Error (RMSE), relative Root Mean Square Error (RMSE%), and Nash–Sutcliffe efficiency coefficient ($E$), were computed. These evaluation metrics have been widely used to estimate the predicative power of regression models (Elarab et al., 2015; Yi et al., 2014). The computation of RMSE, RMSE%, and $E$ are given in Eqs. ((8)–(10)), respectively:

$$\text{RMSE} = \frac{\sqrt{\sum_{i=1}^{S}(\hat{y}_i - y_i)^2}}{S} \tag{8}$$

$$\text{RMSE\%} = 100 * \frac{RMSE}{\bar{y}_i} \tag{9}$$

$$E = 1 - \frac{\sum_{i=1}^{S}(\hat{y}_i - y_i)^2}{\sum_{i=1}^{S}(y_i - \bar{y}_i)^2} \tag{10}$$

where $y_i$ and $\hat{y}_i$ are the measured and the predicted parameters, respectively. $\bar{y}_i$ is the mean of measured parameters, and $S$ is the total number of testing samples. Smaller values of RMSE, RMSE%, and larger values of $E(\infty < E \leqslant 1)$ indicate better precision and accuracy of the prediction model.

To validate the effectiveness of ELR, we compared its performance with two popular regression methods: Support Vector Regression (SVR) (Schölkopf and Smola, 2002; Smola and Schölkopf, 2004) and Partial Least Squares Regression (PLSR) (Geladi and Kowalski, 1986; Hansen and Schjoerring, 2003). For SVR, Sequential Minimal Optimization (SMO) (Fan et al., 2005) was used to solve quadratic programming, and we considered the linear SVR model since ELR was also implemented without any kernel function in our experiments. In PLSR, choosing the Number of Components (NC) is a key step to obtain a successful model, thus we varied the NC from 1 to 6 based on available input variables (features) in the data, and then determined the optimal NC to estimate bio-physicochemical parameters. Results indicated that better accuracy for predicting LAI, FB, and DB was achieved with NC = 3, but NC = 6 was a better choice for retrieving Chl $a$, Chl $b$, Chl $a + b$, and N when considering all combinations of data features. Finally in ELR, the regularization parameter and the number of hidden nodes were tuned empirically from the range $\{2^{-24}, 2^{-23}, \ldots, 2^{24}, 2^{25}\}$ and $\{20, 40, 60, \ldots, 200\}$, respectively. In addition, the sigmoid function $f(x) = 1/(1 + e^x)$ was used as the activation function in ELR for all experiments. The performance of all models was evaluated with averaged RMSE, RMSE% and $E$ over ten different trials.

All the methods were implemented in MATLAB R2016b and run on a 3-GHz desktop computer with an Intel Xeon CPU and 256-GB RAM. Except the implementation code of ELR is the from the ELM website (*http://www.ntu.edu.sg/home/egbhuang/elm_codes.html*), all other competing methods are from the associated MATLAB packages.

## 4. Results

*4.1. Correlations between plant phenotypes and vegetation indices*

Table 4 summarizes the relationships between soybean phenotypic traits and remote sensing indices extracted from UAS imageries using Pearson coefficients (r) available with IBM SPSS software (version 24, IBM Corp., Armonk, NY, US). Correlation coefficients varied between 0.213 and 0.842 ($p < .05$), indicating from moderate to strong correlations between data from field measurements and UAS imagery-based indices. In general, vegetative parameters were negatively correlated with individual red (R), green (G), and blue (B) bands and calculated color indices based on the RGB Sony camera, as well as red and green bands based on the MSI Parrot Sequoia. In contrast, spectral indices calculated from MSI Parrot Sequoia bands generally were positively correlated with vegetative parameters. Moreover, very similar correlation pattern were observed for red and green bands of RGB Sony and MSI Parrot Sequoia cameras, yet the red and green bands from the RGB Sony camera tended to be more strongly correlated (higher r values) with related soybean parameters than those from the MSI Parrot Sequoia. One exception was that the Sony green band was relatively well correlated with DB ($r = -0.501$, $p < .01$), while there was no significant correlation between the MSI Parrot Sequoia green band and DB. For Chl $a$, the highest r value ($r = 0.675$, $p < .01$) was found for GNDVI, though NDRE and the Sony camera G band were still highly correlated with Chl $a$ ($r = 0.646$, $p < .01$ and $r = -0.617$, $p < .01$, respectively). Relatively low correlations ($0.20 < r < 0.44$) were observed between Chl $b$ and UAS data, and the most highly correlated index with Chl $b$ was IPCA ($r = -0.436$, $p < .01$). When Chl $a$ and Chl $b$ were combined, GNDVI was the most strongly correlated with Chl $a + b$ ($r < 0.604$, $p < .01$). Regarding N concentration, while the RGB Sony blue and red band did not show strong correlations ($r < 0.3$), all other UAS indices were strongly correlated with N and the best performance was observed for

**Table 4**
Pearson's correlation coefficient (r) between vegetation parameters and indices. R, G, and B represent red, green, and blue bands of RGB sensor, respectively. INT is color intensity index, IKAW is Kawashima index, IPCA is principal component analysis index, PH is plant height, VF is vegetation fraction; Green, Red, RE and NIR represent green, red, red-edge and near-infrared bands of multispectral sensor. NDVI is normalized difference vegetation index, GNDVI is green normalized difference vegetation index, NDRE is normalized difference red-edge index; Tc is plant canopy temperature.

| Sensor/Info. Types | | Indices | Biochemical Parameters | | | | Biophysical Parameters | | |
|---|---|---|---|---|---|---|---|---|---|
| | | | Chl *a* | Chl *b* | Chl *a* + *b* | N | LAI | FB | DB |
| RGB | Color Info. | R | −0.592** | −0.306** | −0.537** | −0.592** | −0.842** | −0.623** | NS |
| | | G | −0.617** | −0.317** | −0.558** | −0.746** | −0.664** | −0.687** | −0.501* |
| | | B | −0.398** | NS | −0.282** | −0.289** | −0.703** | NS | NS |
| | | INT | −0.560** | −0.248** | −0.484** | −0.588** | −0.791** | −0.620** | NS |
| | | IKAW | −0.317** | −0.355** | −0.394** | −0.562** | NS | −0.477* | −0.616** |
| | | IPCA | −0.549** | −0.436** | −0.583** | −0.617** | −0.805** | −0.696** | −0.598** |
| | Structural Info. | PH | / | / | / | / | 0.664** | 0.736** | 0.669** |
| | | VF | / | / | / | / | 0.811** | 0.583* | NS |
| MSI (Spectral info.) | | Green | −0.520** | −0.282** | −0.479** | −0.766** | −0.503* | −0.595** | NS |
| | | Red | −0.540** | −0.213* | −0.453** | −0.645** | −0.608** | −0.434* | NS |
| | | RE | NS | NS | NS | −0.265** | 0.557** | NS | NS |
| | | NIR | 0.551** | 0.245** | 0.477** | 0.594** | 0.809** | NS | NS |
| | | NDVI | 0.577** | 0.255** | 0.499** | 0.639** | 0.758** | NS | NS |
| | | GNDVI | 0.675** | 0.334** | 0.604** | 0.765** | 0.727** | 0.517** | NS |
| | | NDRE | 0.646** | 0.347** | 0.593** | 0.872** | 0.579** | 0.520** | 0.448* |
| Thermal (Temperature Info.) | | Tc | −0.407** | −0.275** | −0.405** | −0.410** | −0.707** | −0.725** | −0.588** |

Info. represents information; NS represents not significant correlation with p-value < .05. "/" means PH and VF were not used as input features for the biochemical parameters estimation.
** Correlation is significant at the .01 level.
* Significant at the .05 level (2-tailed).

MSI Parrot Sequoia green, GNDVI and NDRE with r values greater than 0.7 ($p < .01$). LAI correlated ($r > 0.55$) with all indices except for IKAW, and the Sony red band had the strongest correlation with LAI ($r = -0.842$, $p < .01$). Evidently, less frequent yet strong correlations were observed for biomass related parameters such as FB and DB.

Plant height estimated from RGB imagery showed the highest r value to both FB and DB ($r = 0.73$, $p < .01$ and $r = 0.669$, $p < .01$, respectively). Vegetation fraction extracted from RGB imagery showed strong correlations with LAI and FB, and the correlation relationship with DB is not statistically significant. RGB imagery based structural information plant height and vegetation fraction were not used as input features for plant biochemical traits estimation in this study, so their correlation relationship were not evaluated.

### 4.2. Modelling and validation of phenotypes

Extreme Learning Machine based Regression (ELR), SVR and PLSR methods were employed in phenotype estimation based on extracted vegetation indices from either RGB, MSI, or TR as well as from different combinations of sensors as shown in Tables 5 and 6. To assess the predictive capabilities of the models, RMSE, RMSE%, and *E* were calculated for all of the modelling results. Overall, in comparison with SVR and PLSR, the ELR method provides more accurate estimation of soybean traits in terms of RMSE, RMSE% and E values when considering multi-sensor data fusion (Tables 5 and 6). Support Vector Regression (SVR) and PLSR showed varying estimating performances for different phenotypes and data fusions.

Based on ELR estimates of biochemical plant traits, the MSI data provided the better results for Chl *a*, Chl *a* + *b* and N estimation than the other individual sensors, followed by the RGB sensor (Table 5). However, RGB data, which not only includes color information but also structural information, dramatically improved the estimation results for LAI, FB and DB compared to individual MSI and TR sensor data (Table 6). Examination of different sensor combinations for data fusion showed that the combination of MSI and TR sensors resulted in the best estimate for Chl *a* (smallest RMSE% - 9.9%) and the RGB color information based indices and MSI data fusion exhibited the largest RMSE of 22.6% for Chl *b* estimation. The most accurate estimates of Chl *a* + *b* were obtained from fusion of data from all three sensors (RMSE% - 11.6%) (Table 5). For N concentration estimation, MSI and TR sensor combination provided the best result (smallest RMSE% - 17.1%). However, compared to each individual sensor data, the improvement achieved by sensor fusion was not significant. For plant biophysical traits, the RGB (including both color and structural information based indices) and TR sensor combination provided the smallest RMSE (5.96%) for LAI estimation. For FB and DB estimation, the MSI and TR sensor combination exhibited the best results with minimum RMSE value of 11.3% and 10.2%, respectively. The advantage of MSI and TR data fusion was significant for biomass estimation compared to any single sensor data or any combination of other sensors' data as demonstrated by its smallest RMSE and largest E value (Table 6).

Phenotype estimates from the best model with the best prediction were compared with corresponding measured values using 1:1 scatterplots (Fig. 6). As expected from the low RMSE% and high E values, Chl *a*, FB, DB, and N estimates from imagery and the ground-based measurements were closely related. Similarly, estimated LAI corresponded very well with the measured values (close to 1:1 line). However, the relationships of estimated and ground-based Chl *b* and Chl *a* + *b* data revealed some biases and inferior relationships.

### 4.3. Mapping plant traits

Plant biophysical and biochemical variables were mapped using the best prediction model for each plant trait (Fig. 7). Visually, the maps of the predicted phenotypes showed good agreement with the RGB map of vigorous growth and high density vegetation, low vegetation areas and bare soil patches. In addition, estimation maps show overall good association with different soybean genotypes, i.e., Pana, Dwight and the commercial cultivar. Compared to Pana and Dwight, the commercial check demonstrated overall greater values for the different phenotypes. Estimated Chlorophyll

**Table 5**
Estimated biochemical plant phenotypes using multi-sensor data fusion. Chlorophyll *a*, *b*, *a* + *b*, and nitrogen concentration are represented by Chl *a*, Chl *b*, Chl *a* + *b*, and N; RMSE, RMSE%, and E are root mean square error, relative RMSE and Nash–Sutcliffe efficiency coefficient, respectively; ELR is Extreme Learning Machine based Regression, SVR is Support Vector Regression, PLSR is Partial Least Squares Regression, RMSE is Root Mean Square Error, RMSE% is relative Root Mean Square Error, E is Nash–Sutcliffe efficiency coefficient. The boldface represents the best performance.

| Sensor type | No. of Features | Metrics | Chl *a* | | | Chl *b* | | | Chl *a* + *b* | | | N | | |
|---|---|---|---|---|---|---|---|---|---|---|---|---|---|---|
| | | | ELR | SVR | PLSR | ELR | SVR | PLSR | ELR | SVR | PLSR | ELR | SVR | PLSR |
| RGB | *6* | *RMSE* | 4.025 | 4.462 | 4.465 | 3.863 | 4.261 | 4.230 | 6.711 | 7.071 | 6.979 | 7.836 | 7.805 | 7.872 |
| | | *RMSE%* | 10.771 | 11.929 | 11.938 | 23.150 | 25.536 | 25.356 | 12.417 | 13.081 | 12.901 | 25.654 | 25.572 | 25.797 |
| | | *E* | 0.394 | 0.255 | 0.255 | 0.282 | 0.120 | 0.131 | 0.337 | 0.251 | 0.268 | 0.537 | 0.532 | 0.526 |
| MSI | *6* | *RMSE* | 3.783 | 5.425 | 3.802 | 4.345 | 4.647 | 4.685 | 6.698 | 8.746 | 6.893 | 5.309 | 12.528 | 5.589 |
| | | *RMSE%* | 10.112 | 14.518 | 10.164 | 26.056 | 27.889 | 28.096 | 12.388 | 16.204 | 12.745 | 17.322 | 40.835 | 18.242 |
| | | *E* | 0.454 | −0.077 | 0.450 | 0.088 | −0.041 | −0.068 | 0.329 | −0.110 | 0.284 | 0.789 | −0.154 | 0.766 |
| TR | *1* | *RMSE* | 4.585 | 4.692 | 4.646 | 4.402 | 4.472 | 4.464 | 7.396 | 7.541 | 7.490 | 8.299 | 9.061 | 9.044 |
| | | *RMSE%* | 12.267 | 12.559 | 12.430 | 26.398 | 26.803 | 26.771 | 13.688 | 13.963 | 13.861 | 27.183 | 29.678 | 29.619 |
| | | *E* | 0.228 | 0.192 | 0.203 | 0.068 | 0.039 | 0.042 | 0.204 | 0.173 | 0.181 | 0.482 | 0.381 | 0.384 |
| MSI + TR | *7* | *RMSE* | **3.715** | 4.670 | 3.781 | 4.163 | 4.470 | 4.667 | 6.391 | 7.537 | 6.683 | **5.227** | 9.008 | 5.595 |
| | | *RMSE%* | **9.930** | 12.498 | 10.107 | 24.949 | 26.794 | 27.974 | 11.818 | 13.955 | 12.357 | **17.070** | 29.503 | 18.257 |
| | | *E* | **0.475** | 0.199 | 0.453 | 0.163 | 0.039 | −0.055 | 0.389 | 0.174 | 0.328 | **0.795** | 0.388 | 0.765 |
| RGB + TR | *7* | *RMSE* | 3.782 | 4.439 | 4.504 | 3.805 | 4.249 | 4.235 | 6.415 | 7.105 | 7.054 | 7.052 | 7.603 | 7.658 |
| | | *RMSE%* | 10.113 | 11.867 | 12.043 | 22.809 | 25.467 | 25.384 | 11.861 | 13.141 | 13.041 | 23.088 | 24.920 | 25.100 |
| | | *E* | 0.459 | 0.264 | 0.242 | 0.302 | 0.126 | 0.128 | 0.388 | 0.241 | 0.253 | 0.623 | 0.557 | 0.550 |
| RGB + MSI | *7* | *RMSE* | 3.938 | 4.444 | 4.299 | **3.778** | 4.260 | 4.396 | 6.564 | 7.079 | 6.817 | 7.599 | 7.777 | 6.515 |
| | | *RMSE%* | 10.535 | 11.881 | 11.494 | **22.634** | 25.528 | 26.356 | 12.142 | 13.096 | 12.604 | 24.878 | 25.480 | 21.339 |
| | | *E* | 0.422 | 0.261 | 0.302 | **0.311** | 0.121 | 0.056 | 0.363 | 0.249 | 0.299 | 0.562 | 0.536 | 0.678 |
| RGB + MSI + TR | *13* | *RMSE* | 3.774 | 4.429 | 4.497 | 3.797 | 4.245 | 4.234 | **6.294** | 7.104 | 7.049 | 6.613 | 7.570 | 7.611 |
| | | *RMSE%* | 10.095 | 11.841 | 12.024 | 22.752 | 25.443 | 25.379 | **11.639** | 13.140 | 13.032 | 21.640 | 24.812 | 24.952 |
| | | *E* | 0.465 | 0.267 | 0.244 | 0.305 | 0.127 | 0.129 | **0.409** | 0.242 | 0.254 | 0.672 | 0.560 | 0.555 |

**Table 6**
Estimated biophysical plant phenotypes using multi-sensor data fusion. Leaf area index, above ground fresh biomass and dry biomass are represented by LAI, FB and DB; RMSE, RMSE%, and E are root mean square error, relative root mean square error and Nash–Sutcliffe efficiency coefficient, respectively. ELR is Extreme Learning Machine based Regression, SVR is Support Vector Regression, PLSR is Partially Least Square Regression.

| Sensor type | No. of features | Metrics | LAI | | | FB | | | DB | | |
|---|---|---|---|---|---|---|---|---|---|---|---|
| | | | ELR | SVR | PLSR | ELR | SVR | PLSR | ELR | SVR | PLSR |
| RGB | *8* | *RMSE* | 0.305 | 0.721 | 0.583 | 200.150 | 289.681 | 318.917 | 40.907 | 62.164 | 62.260 |
| | | *RMSE%* | 6.428 | 15.298 | 12.377 | 13.234 | 19.114 | 21.082 | 12.188 | 18.443 | 18.472 |
| | | *E* | 0.895 | 0.444 | 0.569 | 0.452 | −0.282 | −0.616 | 0.369 | −0.426 | −0.722 |
| MSI | *7* | *RMSE* | 0.742 | 1.257 | 0.834 | 253.632 | 303.166 | 324.209 | 54.978 | 62.333 | 66.266 |
| | | *RMSE%* | 15.613 | 26.901 | 17.556 | 16.753 | 20.074 | 21.392 | 16.313 | 18.512 | 19.740 |
| | | *E* | 0.288 | −0.555 | 0.151 | 0.121 | −0.229 | −0.514 | −0.156 | −0.477 | −0.784 |
| TR | *1* | *RMSE* | 0.866 | 0.956 | 0.922 | 204.676 | 298.457 | 233.188 | 51.419 | 60.860 | 59.224 |
| | | *RMSE%* | 18.375 | 20.376 | 19.526 | 13.558 | 19.754 | 15.526 | 15.231 | 18.053 | 17.604 |
| | | *E* | 0.119 | 0.019 | −0.027 | 0.409 | −0.197 | 0.198 | −0.024 | −0.484 | −0.457 |
| MSI + TR | *8* | *RMSE* | 0.621 | 0.947 | 0.735 | **170.904** | 298.448 | 235.879 | **34.229** | 60.858 | 53.508 |
| | | *RMSE%* | 13.118 | 20.181 | 15.517 | **11.341** | 19.754 | 15.718 | **10.229** | 18.053 | 15.941 |
| | | *E* | 0.549 | 0.047 | 0.339 | **0.573** | −0.197 | 0.176 | **0.538** | −0.484 | −0.230 |
| RGB + TR | *9* | *RMSE* | **0.284** | 0.755 | 0.583 | 207.290 | 289.000 | 320.482 | 41.625 | 62.248 | 63.887 |
| | | *RMSE%* | **5.961** | 16.028 | 12.361 | 13.673 | 19.073 | 21.185 | 12.376 | 18.474 | 18.934 |
| | | *E* | **0.882** | 0.410 | 0.57 | 0.394 | −0.277 | −0.632 | 0.377 | −0.428 | −1.000 |
| RGB + MSI | *15* | RMSE | 0.305 | 0.722 | 0.583 | 187.710 | 290.124 | 318.921 | 40.755 | 62.178 | 62.260 |
| | | RMSE% | 6.402 | 15.311 | 12.377 | 12.377 | 19.144 | 21.082 | 12.138 | 18.448 | 18.472 |
| | | E | 0.876 | 0.446 | 0.569 | 0.463 | −0.286 | −0.616 | 0.423 | −0.426 | −0.722 |
| RGB + MSI+TR | *16* | RMSE | 0.314 | 0.755 | 0.583 | 207.547 | 289.476 | 320.48 | 36.044 | 62.282 | 63.886 |
| | | RMSE% | 6.585 | 16.023 | 12.361 | 13.700 | 19.106 | 21.185 | 10.718 | 18.483 | 18.934 |
| | | E | 0.857 | 0.410 | 0.570 | 0.373 | −0.280 | −0.632 | 0.471 | −0.429 | −1.000 |

content and N concentration maps exhibited very similar patterns. Not surprisingly, FB and DB maps also resembled each other.

## 5. Discussion

Partial Least Squares Regression (PLSR) is one of the popular methods used in estimating plant biophysical and/or biochemical variables (Hansen and Schjoerring, 2003; Rischbeck et al., 2016). In recent years, regression methods based on machine learning techniques (e.g., SVR, neural network) has become attractive due to its robustness in various regression analysis (Camps-Valls et al., 2006; Elarab et al., 2015; Tuia et al., 2011; Walthall et al., 2004). This contribution applied ELR, a relatively new machine learning algorithm and in phenotype traits estimation for the first time, and compared its advantages against most common conventional regression methods including PLSR and SVR. Relative to PLSR and SVR methods, ELR is more capable to handle complex data from various sensors based on the experimental results in this

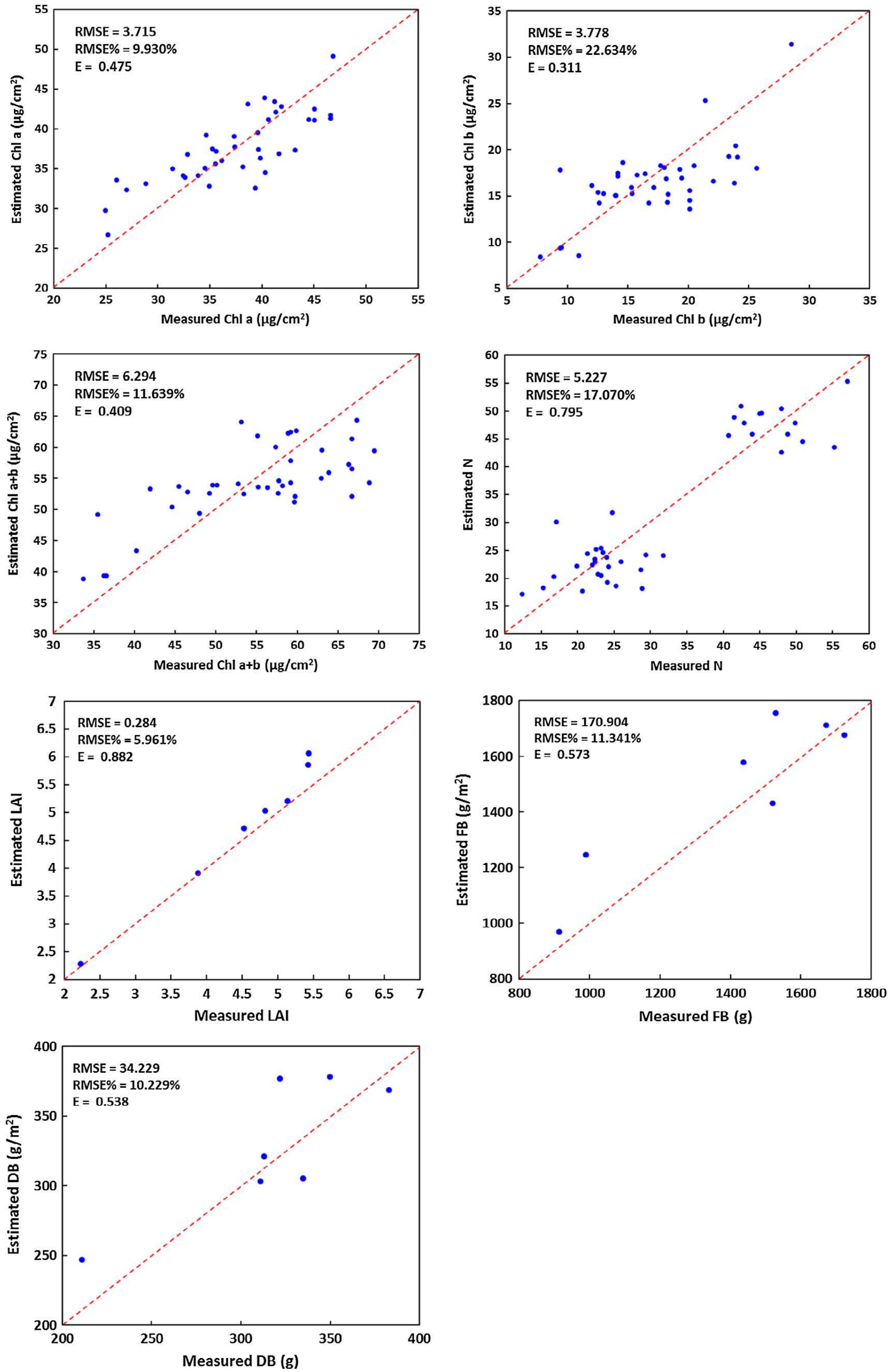


**Fig. 6.** Measured vs. predicted plant phenotypes using ELR based multi-sensor data fusion.

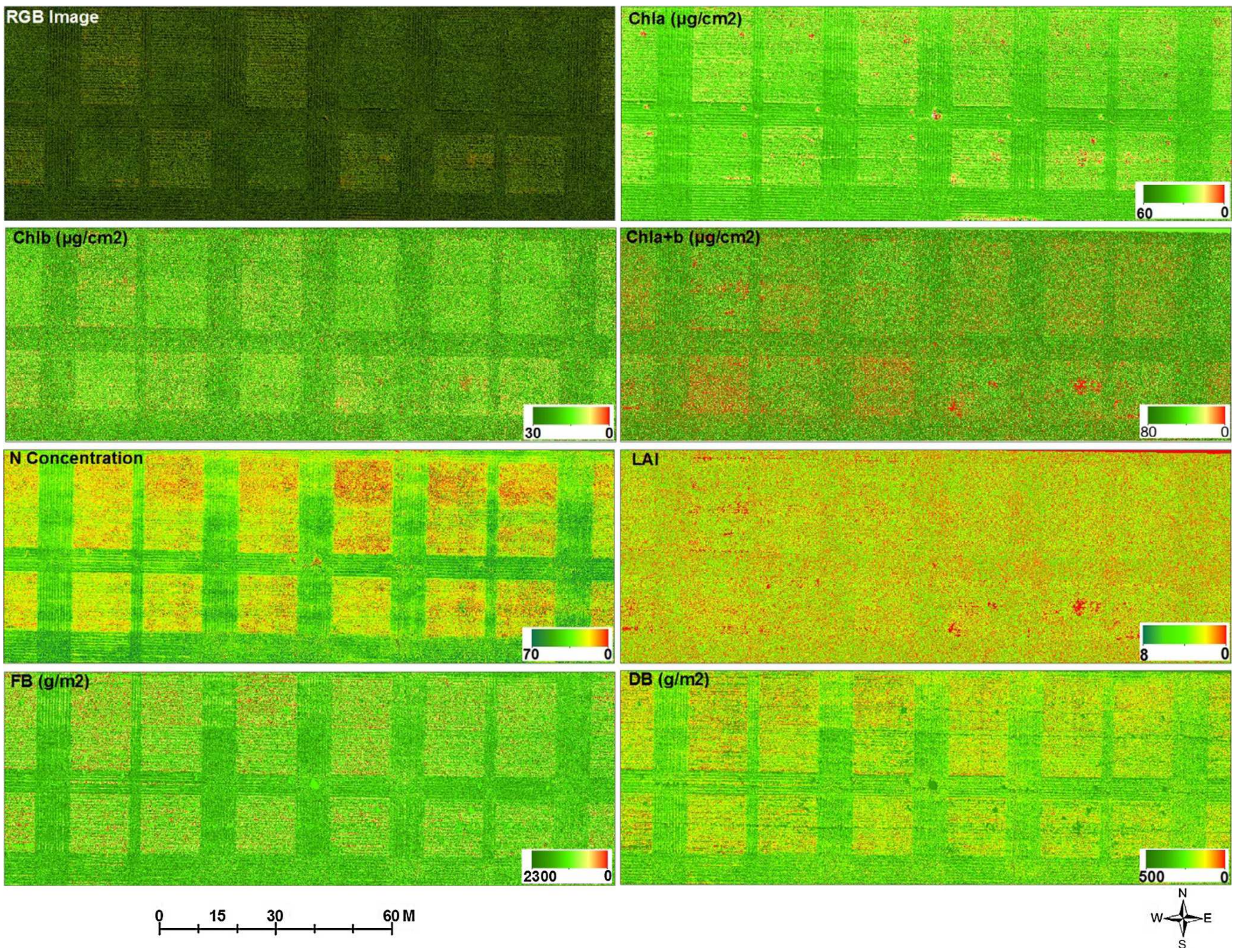


**Fig. 7.** Plant phenotyping traits estimation map using ELR based multi-sensor data fusion.

study. Extreme Learning Machine based Regression (ELR) not only tends to reach the minimum training error but also the smallest norm of weights, which ensures ELR has better generalization performance (Ding et al., 2015; Huang et al., 2012). Another reason for using ELR is the fast learning property achieved by randomly assigning the input weights and hidden layer biases, which makes it suitable for real-time training (Huang et al., 2006). For these reasons, our discussion below will focus on the results of ELR based estimation.

RGB and MSI data both provide spectral information in the VIS region. Additionally, Parrot Sequoia MSI data also cover NIR and red-edge bands, and the TR sensor provides information from the 8 to 14 μm range. Comparison of single sensor phenotype estimates revealed that MSI data performed better for chlorophyll and N prediction than RGB data (Table 5). This may be due to the contribution of NIR spectral information in biochemical traits estimation, because NIR band contains information on both the physiological status and the geometric properties of vegetation (Cozzolino et al., 2001; Curran, 1989; Houborg and Boegh, 2008; Knipling, 1970). This was consistent with previous studies that reported the importance of NIR information for plant trait estimations (Berni et al., 2009; Lebourgeois et al., 2012; Zaman-Allah et al., 2015; Zhang and Kovacs, 2012). However, the RGB data, which includes VIS spectral and canopy structural information, outperformed MSI data for LAI and biomass estimation (Table 6). This could be due to the saturation issue associated with VIS-NIR sensor for dense vegetation. Our results showed that coupled spectral and structural information could overcome saturation issue to some extent, which was consistent with the conclusion of previous studies (Huete et al., 2002; Thenkabail et al., 2000; Tilly et al., 2015; Wang et al., 2016). Further, although thermal data based estimation did not outperform RGB and MSI data, the estimation capability based on TR sensor data was comparable to RGB and MSI data for at least some of the plant traits (Tables 5 and 6). This is not surprising since variations in leaf chlorophyll concentration and N concentration can result in differences in canopy temperature (da Luz and Crowley, 2010; Elarab et al., 2015). In addition, bare soil and vegetation fraction in crop fields also contributes to canopy temperature variance (Kustas and Norman, 1999; Mo et al., 1982; Neinavaz et al., 2016). Clearly, canopy temperature is strongly influenced by a broad range of environmental conditions, including water availability (Blum et al., 1982), and much additional research is needed to better understand the relationships of canopy temperature and various plant traits with respect to a variety of factors including plant developmental stage, diurnal responses, environmental conditions and their interactions.

Phenotype estimations were also obtained based on data fusion from different sensor combinations (MSI + TR, RGB + TR, RGB + MSI, and RGB + MSI + TR) and were compared to the estimates based on single sensor data. Overall, the accuracies of sensor fusion based phenotype estimates were greater than phenotype estimates based on data from single sensors. Data fusion based on all three sensors simultaneously outperformed combination of any two sensors only for prediction of Chl $a+b$ (Table 5). This may be associated with information redundancy issues caused by the fusion of multiple sources of data (Pohl and Van Genderen, 1998).

Data fusion based on the different two-sensor combinations generally resulted in very similar performance. RGB and MSI have similar information in the VIS spectral region that would lead to information overlap and further impact the predicting capability (Dong et al., 2009; Luo et al., 2015), but nonetheless provided the best estimation for Chl *b* (Table 5). RGB and MSI fusion also outperformed any single sensor in predicting biophysical traits (Table 6), which may due to mutual complementation of both structural and spectral information (Reddersen et al., 2014; Schaefer and Lamb, 2016; Schirrmann et al., 2016).

MSI and TR fusion which includes VIS-NIR spectra and canopy temperature information provided the best estimates for Chl *a*, N, FB and DB. Compared to MSI and RGB, MSI and thermal fusion suffer less information overlap such that thermal data better complement information derived from MSI data (Elarab et al., 2015; Prashar and Jones, 2014). RGB and thermal fusion, which combines color, canopy structure and temperature information, resulted in the best prediction for LAI (Table 6). This is likely due to the minimized saturation effect of optical remote sensing by canopy structural and temperature information, which complements spectral information for the estimation of LAI (Chianucci et al., 2016; Manninen et al., 2009; Mathews and Jensen, 2013).

Consistent with previous studies (Luo et al., 2017; Muharam et al., 2015; Schaefer and Lamb, 2016; Wang et al., 2016), coupling structural and spectral information improved the accuracy of LAI and biomass estimation in this study. Combining thermal with RGB or MSI data outperformed spectral and structural information fusion from RGB and MSI for LAI, biomass, Chl *a*, and N prediction. This finding implies that thermal data provides value that has not been fully explored for biochemical and biophysical plant trait estimations.

## 6. Conclusion

Rapid advances in sensor technology, unmanned aerial systems, and computing power have facilitated exponential growth in remote sensing applications with multi-sensor data fusion. One of these development frontiers is automated high-throughput crop phenotyping using low-cost aerial images for estimating biophysical and biochemical plant parameters. This paper evaluated the contribution of RGB, multispectral, and thermal data and fusions of different combinations of these data to estimate crop biochemical (chlorophyll content and N concentration) and biophysical (LAI, fresh and dry biomass) traits. The main conclusions resulting from this study include:

1) In prediction of the soybean traits from multi-sensor data fusion, ELR demonstrates relatively superior performance compared to PLSR and SVR in this study.
2) Multispectral and thermal data fusion provided the best estimate for N concentration and chlorophyll *a*. In contrast, RGB color information based indices and multispectral data fusion exhibited the largest RMSE% (22.6%). Fusion of all three sensors outperformed combination of any two sensors as well as single sensors for prediction of Chl $a+b$ (smallest RMSE% - 11.6%).
3) Among the plant biophysical traits, RGB and thermal data fusion, which combines color, canopy structure and temperature information, resulted in best prediction for LAI while multispectral and thermal data fusion was found to be best for biomass estimation.

The results from this study demonstrate that fusion of low-cost multiple sensor data within a machine learning framework can provide relative accurate estimation of plant phenotypes. It is worth mentioning that data fusion can improve the accuracy of phenotype estimates; however, to identify the most accurate and efficient combination sensor data for fusion, more comprehensive studies are necessary, including studies on different crop species. In addition, data fusion does not always improve prediction accuracy dramatically. Thus, a tradeoff between accuracy improvement and cost of using multiple sensors should be considered for a specific application.

## Acknowledgements

Funding for this work was provided by National Science Foundation (IIA-1355406 and IIA-1430427), NASA (NNX15AK03H), and the Center for Sustainability at Saint Louis University. The authors thank Missouri EPSCoR researchers who contributed long and strenuous hours to collect field data. The authors also thank the editor and the anonymous reviewers for their thoughtful review and constructive comments.

## References

Ahmad, I.S., Reid, J.F., 1996. Evaluation of colour representations for maize images. J. Agric. Eng. Res. 63, 185–195.
Alom, M.Z., Sidike, P., Taha, T.M., Asari, V.K., 2016. State preserving extreme learning machine: a monotonically increasing learning approach. Neural Process. Lett., 1–23
Araus, J.L., Cairns, J.E., 2014. Field high-throughput phenotyping: the new crop breeding frontier. Trends Plant Sci. 19, 52–61.
Barnes, E., Clarke, T., Richards, S., Colaizzi, P., Haberland, J., Kostrzewski, M., Waller, P., Choi, C., Riley, E., Thompson, T., 2000. Coincident detection of crop water stress, nitrogen status and canopy density using ground based multispectral data. In: Proceedings of the 5th International Conference on Precision Agriculture, Bloomington, MN, pp. 16–19.
Bendig, J., Bolten, A., Bennertz, S., Broscheit, J., Eichfuss, S., Bareth, G., 2014. Estimating biomass of barley using crop surface models (CSMs) derived from UAV-based RGB imaging. Remote Sens.-Basel 6, 10395–10412.
Bendig, J., Yu, K., Aasen, H., Bolten, A., Bennertz, S., Broscheit, J., Gnyp, M.L., Bareth, G., 2015. Combining UAV-based plant height from crop surface models, visible, and near infrared vegetation indices for biomass monitoring in barley. Int. J. Appl. Earth Obs. 39, 79–87.
Berni, J.A., Zarco-Tejada, P.J., Suárez, L., Fereres, E., 2009. Thermal and narrowband multispectral remote sensing for vegetation monitoring from an unmanned aerial vehicle. IEEE Trans. Geosci. Remote 47, 722–738.
Bilger, W., Johnsen, T., Schreiber, U., 2001. UV-excited chlorophyll fluorescence as a tool for the assessment of UV-protection by the epidermis of plants. J. Exp. Bot. 52, 2007–2014.
Blum, A., Mayer, J., Gozlan, G., 1982. Infrared thermal sensing of plant canopies as a screening technique for dehydration avoidance in wheat. Field Crop Res. 5, 137–146.
Breda, N.J.J., 2003. Ground-based measurements of leaf area index: a review of methods, instruments and current controversies. J. Exp. Bot. 54, 2403–2417.
Camps-Valls, G., Bruzzone, L., Rojo-Álvarez, J.L., Melgani, F., 2006. Robust support vector regression for biophysical variable estimation from remotely sensed images. IEEE Geosci. Remote Sci. 3, 339–343.
Cartelat, A., Cerovic, Z.G., Goulas, Y., Meyer, S., Lelarge, C., Prioul, J.L., Barbottin, A., Jeuffroy, M.H., Gate, P., Agati, G., Moya, I., 2005. Optically assessed contents of leaf polyphenolics and chlorophyll as indicators of nitrogen deficiency in wheat (*Triticum aestivum* L.). Field Crop Res. 91, 35–49.
Caturegli, L., Corniglia, M., Gaetani, M., Grossi, N., Magni, S., Migliazzi, M., Angelini, L., Mazzoncini, M., Silvestri, N., Fontanelli, M., Raffaelli, M., Peruzzi, A., Volterrani, M., 2016. Unmanned aerial vehicle to estimate nitrogen status of turfgrasses. Plos One 11.
Cerovic, Z.G., Masdoumier, G., Ben Ghozlen, N., Latouche, G., 2012. A new optical leaf-clip meter for simultaneous non-destructive assessment of leaf chlorophyll and epidermal flavonoids. Physiol. Plant. 146, 251–260.
Chao, H., Coopmans, C., Di, L., Chen, Y., 2010. A comparative evaluation of low-cost IMUs for unmanned autonomous systems. In: 2010 IEEE Conference on Multisensor Fusion and Integration for Intelligent Systems (MFI). IEEE, pp. 211–216.
Chen, Y., Yao, E., Basu, A., 2016. A 128-channel extreme learning machine-based neural decoder for brain machine interfaces. IEEE Trans. Biomed. Circuits Syst. 10, 679–692.
Chianucci, F., Disperati, L., Guzzi, D., Bianchini, D., Nardino, V., Lastri, C., Rindinella, A., Corona, P., 2016. Estimation of canopy attributes in beech forests using true

colour digital images from a small fixed-wing UAV. Int. J. Appl. Earth Obs. 47, 60–68.
Cipollini, P., Corsini, G., Diani, M., Grasso, R., 2001. Retrieval of sea water optically active parameters from hyperspectral data by means of generalized radial basis function neural networks. IEEE Trans. Geosci. Remote Sens. 39, 1508–1524.
Corcoles, J.I., Ortega, J.F., Hernandez, D., Moreno, M.A., 2013. Estimation of leaf area index in onion (*Allium cepa* L.) using an unmanned aerial vehicle. Biosys. Eng. 115, 31–42.
Cortes, C., Vapnik, V., 1995. Support-vector networks. Mach. Learning 20, 273–297.
Cozzolino, D., Fassio, A., Gimenez, A., 2001. The use of near-infrared reflectance spectroscopy (NIRS) to predict the composition of whole maize plants. J. Sci. Food Agric. 81, 142–146.
Curran, P.J., 1989. Remote sensing of foliar chemistry. Remote Sens. Environ. 30, 271–278.
da Luz, B.R., Crowley, J.K., 2010. Identification of plant species by using high spatial and spectral resolution thermal infrared (8.0–13.5 μm) imagery. Remote Sens. Environ. 114, 404–413.
Demmigadams, B., Adams, W.W., 1992. Photoprotection and other responses of plants to high light stress. Annu. Rev. Plant Phys. 43, 599–626.
Ding, S.F., Zhao, H., Zhang, Y.N., Xu, X.Z., Nie, R., 2015. Extreme learning machine: algorithm, theory and applications. Artif. Intell. Rev. 44, 103–115.
Dong, J., Zhuang, D., Huang, Y., Fu, J., 2009. Advances in multi-sensor data fusion: algorithms and applications. Sensors-Basel 9, 7771–7784.
Du, W.Y., Zhang, L.D., Hu, Z.F., Shamaila, Z., Zeng, A.J., Song, J.L., Liu, Y.J., Wolfram, S., Joachim, M., He, X.K., 2011. Utilization of thermal infrared image for inversion of winter wheat yield and biomass. Spectrosc. Spect. Anal. 31, 1476–1480.
Ehrler, W.L., 1973. Cotton leaf temperatures as related to soil water depletion and meteorological factors. Agron. J. 65, 404–409.
Elarab, M., Ticlavilca, A.M., Torres-Rua, A.F., Maslova, I., McKee, M., 2015. Estimating chlorophyll with thermal and broadband multispectral high resolution imagery from an unmanned aerial system using relevance vector machines for precision agriculture. Int. J. Appl. Earth Obs. 43, 32–42.
Fan, R.-E., Chen, P.-H., Lin, C.-J., 2005. Working set selection using second order information for training support vector machines. J. Mach. Learning Res. 6, 1889–1918.
Fichtner, K., Schulze, E.-D., 1992. The effect of nitrogen nutrition on growth and biomass partitioning of annual plants originating from habitats of different nitrogen availability. Oecologia 92, 236–241.
Furbank, R.T., Tester, M., 2011. Phenomics - technologies to relieve the phenotyping bottleneck. Trends Plant Sci. 16, 635–644.
Galvao, L.S., Breunig, F.M., dos Santos, J.R., de Moura, Y.M., 2013. View-illumination effects on hyperspectral vegetation indices in the Amazonian tropical forest. Int. J. Appl. Earth Obs. 21, 291–300.
Gamon, J.A., Surfus, J.S., 1999. Assessing leaf pigment content and activity with a reflectometer. New Phytol. 143, 105–117.
Gastal, F., Lemaire, G., 2002. N uptake and distribution in crops: an agronomical and ecophysiological perspective. J. Exp. Bot. 53, 789–799.
Geipel, J., Link, J., Claupein, W., 2014. Combined spectral and spatial modeling of corn yield based on aerial images and crop surface models acquired with an unmanned aircraft system. Remote Sens.-Basel 6, 10335–10355.
Geladi, P., Kowalski, B.R., 1986. Partial least-squares regression: a tutorial. Anal. Chim. Acta 185, 1–17.
Gitelson, A.A., Kaufman, Y.J., Merzlyak, M.N., 1996. Use of a green channel in remote sensing of global vegetation from EOS-MODIS. Remote Sens. Environ. 58, 289–298.
Gitelson, A.A., Vina, A., Verma, S.B., Rundquist, D.C., Arkebauer, T.J., Keydan, G., Leavitt, B., Ciganda, V., Burba, G.G., Suyker, A.E., 2006. Relationship between gross primary production and chlorophyll content in crops: implications for the synoptic monitoring of vegetation productivity. J. Geophys. Res.-Atmos. 111.
Gökkaya, K., Thomas, V., Noland, T.L., McCaughey, H., Morrison, I., Treitz, P., 2015. Prediction of macronutrients at the canopy level using spaceborne imaging spectroscopy and LiDAR data in a mixedwood boreal forest. Remote Sens.-Basel 7, 9045–9069.
Gonzalez-Dugo, V., Hernandez, P., Solis, I., Zarco-Tejada, P.J., 2015. Using high-resolution hyperspectral and thermal airborne imagery to assess physiological condition in the context of wheat phenotyping. Remote Sens.-Basel 7, 13586–13605.
Goulas, Y., Cerovic, Z.G., Cartelat, A., Moya, I., 2004. Dualex: a new instrument for field measurements of epidermal ultraviolet absorbance by chlorophyll fluorescence. Appl. Opt. 43, 4488–4496.
Guo, J.X., Tian, G.L., Zhou, Y., Wang, M., Ling, N., Shen, Q.R., Guo, S.W., 2016. Evaluation of the grain yield and nitrogen nutrient status of wheat (*Triticum aestivum* L.) using thermal imaging. Field Crop Res. 196, 463–472.
Haghighattalab, A., Perez, L.G., Mondal, S., Singh, D., Schinstock, D., Rutkoski, J., Ortiz-Monasterio, I., Singh, R.P., Goodin, D., Poland, J., 2016. Application of unmanned aerial systems for high throughput phenotyping of large wheat breeding nurseries. Plant Methods 12.
Hansen, P., Schjoerring, J., 2003. Reflectance measurement of canopy biomass and nitrogen status in wheat crops using normalized difference vegetation indices and partial least squares regression. Remote Sens. Environ. 86, 542–553.
Hassan-Esfahani, L., Torres-Rua, A., Jensen, A., McKee, M., 2015. Assessment of surface soil moisture using high-resolution multi-spectral imagery and artificial neural networks. Remote Sens. 7, 2627–2646.
Hauke, J., Kossowski, T., 2011. Comparison of values of Pearson's and Spearman's correlation coefficients on the same sets of data. Quaestiones geographicae 30, 87.
Hofle, B., 2014. Radiometric correction of terrestrial LiDAR point cloud data for individual maize plant detection. IEEE Geosci. Remote Sci. 11, 94–98.
Honkavaara, E., Saari, H., Kaivosoja, J., Polonen, I., Hakala, T., Litkey, P., Makynen, J., Pesonen, L., 2013. Processing and assessment of spectrometric, stereoscopic imagery collected using a lightweight UAV spectral camera for precision agriculture. Remote Sens.-Basel 5, 5006–5039.
Houborg, R., Boegh, E., 2008. Mapping leaf chlorophyll and leaf area index using inverse and forward canopy reflectance modeling and SPOT reflectance data. Remote Sens. Environ. 112, 186–202.
Huang, G.-B., Zhu, Q.-Y., Siew, C.-K., 2006. Extreme learning machine: theory and applications. Neurocomputing 70, 489–501.
Huang, G.B., Zhou, H.M., Ding, X.J., Zhang, R., 2012. Extreme learning machine for regression and multiclass classification. IEEE Trans. Syst. Man Cybernetic B 42, 513–529.
Huete, A., Didan, K., Miura, T., Rodriguez, E.P., Gao, X., Ferreira, L.G., 2002. Overview of the radiometric and biophysical performance of the MODIS vegetation indices. Remote Sens. Environ. 83, 195–213.
Hunt, E., Hively, W.D., Daughtry, C.S., McCarty, G.W., Fujikawa, S.J., Ng, T., Tranchitella, M., Linden, D.S., Yoel, D.W., 2008. Remote sensing of crop leaf area index using unmanned airborne vehicles. In: Proceedings of the Pecora 17 Symposium, Denver CO.
Hunt, E.R., Cavigelli, M., Daughtry, C.S., Mcmurtrey, J.E., Walthall, C.L., 2005. Evaluation of digital photography from model aircraft for remote sensing of crop biomass and nitrogen status. Precision Agric. 6, 359–378.
Kalisperakis, I., Stentoumis, C., Grammatikopoulos, L., Karantzalos, K., 2015. Leaf area index estimation in vineyards from UAV hyperspectral data, 2D image mosaics and 3D canopy surface models. Int. Arch. Photogramm. Remote Sens. Spatial Inf. Sci. 40, 299.
Kawashima, S., Nakatani, M., 1998. An algorithm for estimating chlorophyll content in leaves using a video camera. Ann. Bot. 81, 49–54.
Knipling, E.B., 1970. Physical and physiological basis for the reflectance of visible and near-infrared radiation from vegetation. Remote Sens. Environ. 1, 155–159.
Kustas, W.P., Norman, J.M., 1999. Evaluation of soil and vegetation heat flux predictions using a simple two-source model with radiometric temperatures for partial canopy cover. Agric. For. Meteorol. 94, 13–29.
Lebourgeois, V., Bégué, A., Labbé, S., Houlès, M., Martiné, J.-F., 2012. A light-weight multi-spectral aerial imaging system for nitrogen crop monitoring. Precision Agric. 13, 525–541.
Li, J.W., Zhang, F., Qian, X.Y., Zhu, Y.H., Shen, G.X., 2015. Quantification of rice canopy nitrogen balance index with digital imagery from unmanned aerial vehicle. Remote Sens. Lett. 6, 183–189.
Li, L., Zhang, Q., Huang, D., 2014. A review of imaging techniques for plant phenotyping. Sensors-Basel 14, 20078–20111.
Li, W., Niu, Z., Chen, H.Y., Li, D., Wu, M.Q., Zhao, W., 2016. Remote estimation of canopy height and aboveground biomass of maize using high-resolution stereo images from a low-cost unmanned aerial vehicle system. Ecol. Indic. 67, 637–648.
Lichtenthaler, H.K., 1987. [34] Chlorophylls and carotenoids: pigments of photosynthetic biomembranes. Methods Enzymol. 148, 350–382.
Lichtenthaler, H.K., Buschmann, C., 2001. Chlorophylls and carotenoids: Measurement and characterization by UV-VIS spectroscopy. Current protocols in food analytical chemistry.
Liu, Y., Yang, S.J., Li, S.Q., Chen, X.P., Chen, F., 2010. Growth and development of maize (*Zea mays* L.) in response to different field water management practices: resource capture and use efficiency. Agric. For. Meteorol. 150, 606–613.
Lucieer, A., Turner, D., King, D.H., Robinson, S.A., 2014. Using an Unmanned Aerial Vehicle (UAV) to capture micro-topography of Antarctic moss beds. Int. J. Appl. Earth Obs. 27, 53–62.
Luo, S., Wang, C., Xi, X., Pan, F., Peng, D., Zou, J., Nie, S., Qin, H., 2017. Fusion of airborne LiDAR data and hyperspectral imagery for aboveground and belowground forest biomass estimation. Ecol. Indic. 73, 378–387.
Luo, S., Wang, C., Xi, X., Zeng, H., Li, D., Xia, S., Wang, P., 2015. Fusion of airborne discrete-return LiDAR and hyperspectral data for land cover classification. Remote Sens.-Basel 8, 3.
Manninen, T., Korhonen, L., Voipio, P., Lahtinen, P., Stenberg, P., 2009. Leaf Area Index (LAI) estimation of boreal forest using wide optics airborne winter photos. Remote Sens.-Basel 1, 1380–1394.
Marshall, M., Thenkabail, P., 2015. Developing in situ non-destructive estimates of crop biomass to address issues of scale in remote sensing. Remote Sens.-Basel 7, 808–835.
Martinelli, F., Scalenghe, R., Davino, S., Panno, S., Scuderi, G., Ruisi, P., Villa, P., Stroppiana, D., Boschetti, M., Goulart, L.R., 2015. Advanced methods of plant disease detection. A review. Agron. Sustain. Dev. 35, 1–25.
Masclaux-Daubresse, C., Daniel-Vedele, F., Dechorgnat, J., Chardon, F., Gaufichon, L., Suzuki, A., 2010. Nitrogen uptake, assimilation and remobilization in plants: challenges for sustainable and productive agriculture. Ann. Bot. 105, 1141–1157.
Mathews, A.J., Jensen, J.L., 2013. Visualizing and quantifying vineyard canopy LAI using an unmanned aerial vehicle (UAV) collected high density structure from motion point cloud. Remote Sens.-Basel 5, 2164–2183.
Mistele, B., Schmidhalter, U., 2008. Estimating the nitrogen nutrition index using spectral canopy reflectance measurements. Eur. J. Agron. 29, 184–190.
Mo, T., Choudhury, B., Schmugge, T., Wang, J., Jackson, T., 1982. A model for microwave emission from vegetation-covered fields. J. Geophys. Res.: Oceans 87, 11229–11237.

Mora, M., Avila, F., Carrasco-Benavides, M., Maldonado, G., Olguin-Caceres, J., Fuentes, S., 2016. Automated computation of leaf area index from fruit trees using improved image processing algorithms applied to canopy cover digital photograpies. Comput. Electron Agr. 123, 195–202.

Moreno, R., Corona, F., Lendasse, A., Grana, M., Galvao, L.S., 2014. Extreme learning machines for soybean classification in remote sensing hyperspectral images. Neurocomputing 128, 207–216.

Moser, G., Serpico, S.B., 2009. Automatic parameter optimization for support vector regression for land and sea surface temperature estimation from remote sensing data. IEEE Trans. Geosci. Remote Sens. 47, 909–921.

Muharam, F.M., Maas, S.J., Bronson, K.F., Delahunty, T., 2015. Estimating cotton nitrogen nutrition status using leaf greenness and ground cover information. Remote Sens.-Basel 7, 7007–7028.

Munoz-Huerta, R.F., Guevara-Gonzalez, R.G., Contreras-Medina, L.M., Torres-Pacheco, I., Prado-Olivarez, J., Ocampo-Velazquez, R.V., 2013. A review of methods for sensing the nitrogen status in plants: advantages, disadvantages and recent advances. Sensors-Basel 13, 10823–10843.

Neinavaz, E., Skidmore, A.K., Darvishzadeh, R., Groen, T.A., 2016. Retrieval of leaf area index in different plant species using thermal hyperspectral data. ISPRS J. Photogramm. 119, 390–401.

Peng, Y., Gitelson, A.A., Keydan, G., Rundquist, D.C., Moses, W., 2011. Remote estimation of gross primary production in maize and support for a new paradigm based on total crop chlorophyll content. Remote Sens. Environ. 115, 978–989.

Pohl, C., Van Genderen, J.L., 1998. Review article multisensor image fusion in remote sensing: concepts, methods and applications. Int. J. Remote Sens. 19, 823–854.

Prasertsak, A., Fukai, S., 1997. Nitrogen availability and water stress interaction on rice growth and yield. Field Crop Res. 52, 249–260.

Prashar, A., Jones, H.G., 2014. Infra-red thermography as a high-throughput tool for field phenotyping. Agronomy 4, 397–417.

Primicerio, J., Di Gennaro, S.F., Fiorillo, E., Genesio, L., Lugato, E., Matese, A., Vaccari, F.P., 2012. A flexible unmanned aerial vehicle for precision agriculture. Precision Agric. 13, 517–523.

Rao, C.R., Mitra, S.K., 1971. Generalized Inverse of Matrices and its Applications.

Reddersen, B., Fricke, T., Wachendorf, M., 2014. A multi-sensor approach for predicting biomass of extensively managed grassland. Comput. Electron. Agric. 109, 247–260.

Rey-Carames, C., Diago, M.P., Martin, M.P., Lobo, A., Tardaguila, J., 2015. Using RPAS multi-spectral imagery to characterise vigour, leaf development, yield components and berry composition variability within a vineyard. Remote Sens.-Basel 7, 14458–14481.

Richardson, A.D., Duigan, S.P., Berlyn, G.P., 2002. An evaluation of noninvasive methods to estimate foliar chlorophyll content. New Phytol. 153, 185–194.

Rischbeck, P., Elsayed, S., Mistele, B., Barmeier, G., Heil, K., Schmidhalter, U., 2016. Data fusion of spectral, thermal and canopy height parameters for improved yield prediction of drought stressed spring barley. Eur. J. Agron. 78, 44–59.

Rose, J.C., Paulus, S., Kuhlmann, H., 2015. Accuracy analysis of a multi-view stereo approach for phenotyping of tomato plants at the organ level. Sensors-Basel 15, 9651–9665.

Rouse Jr., J., 1974. Monitoring the vernal advancement and retrogradation (green wave effect) of natural vegetation.

Saberioon, M., Amin, M., Anuar, A., Gholizadeh, A., Wayayok, A., Khairunniza-Bejo, S., 2014. Assessment of rice leaf chlorophyll content using visible bands at different growth stages at both the leaf and canopy scale. Int. J. Appl. Earth Obs. 32, 35–45.

Salami, E., Barrado, C., Pastor, E., 2014. UAV flight experiments applied to the remote sensing of vegetated areas. Remote Sens.-Basel 6, 11051–11081.

Salvucci, M.E., Crafts-Brandner, S.J., 2004. Inhibition of photosynthesis by heat stress: the activation state of Rubisco as a limiting factor in photosynthesis. Physiol. Plant. 120, 179–186.

Sankaran, S., Khot, L.R., Espinoza, C.Z., Jarolmasjed, S., Sathuvalli, V.R., Vandemark, G. J., Miklas, P.N., Carter, A.H., Pumphrey, M.O., Knowles, N.R., Payek, M.J., 2015. Low-altitude, high-resolution aerial imaging systems for row and field crop phenotyping: a review. Eur. J. Agron. 70, 112–123.

Savojardo, C., Fariselli, P., Casadio, R., 2013. BETAWARE: a machine-learning tool to detect and predict transmembrane beta barrel proteins in Prokaryotes. Bioinformatics, bts728.

Schaefer, M.T., Lamb, D.W., 2016. A combination of plant NDVI and LiDAR measurements improve the estimation of pasture biomass in Tall Fescue (*Festuca arundinacea* var. Fletcher). Remote Sens.-Basel 8, 109.

Schirrmann, M., Giebel, A., Gleiniger, F., Pflanz, M., Lentschke, J., Dammer, K.-H., 2016. Monitoring agronomic parameters of winter wheat crops with low-cost UAV imagery. Remote Sens.-Basel 8, 706.

Schölkopf, B., Smola, A.J., 2002. Learning With Kernels: Support Vector Machines, Regularization, Optimization, and Beyond. MIT Press.

Sepulcre-Cantó, G., Zarco-Tejada, P.J., Jimenez-Munoz, J., Sobrino, J., De Miguel, E., Villalobos, F.J., 2006. Detection of water stress in an olive orchard with thermal remote sensing imagery. Agric. For. Meteorol. 136, 31–44.

Serrano, L., Filella, I., Penuelas, J., 2000. Remote sensing of biomass and yield of winter wheat under different nitrogen supplies. Crop Sci. 40, 723–731.

Sharkey, T.D., 2005. Effects of moderate heat stress on photosynthesis: importance of thylakoid reactions, rubisco deactivation, reactive oxygen species, and thermotolerance provided by isoprene. Plant Cell Environ. 28, 269–277.

Shi, Y.Y., Thomasson, J.A., Murray, S.C., Pugh, N.A., Rooney, W.L., Shafian, S., Rajan, N., Rouze, G., Morgan, C.L.S., Neely, H.L., Rana, A., Bagavathiannan, M.V., Henrickson, J., Bowden, E., Valasek, J., Olsenholler, J., Bishop, M.P., Sheridan, R., Putman, E.B., Popescu, S., Burks, T., Cope, D., Ibrahim, A., McCutchen, B.F., Baltensperger, D.D., Avant, R.V., Vidrine, M., Yang, C.H., 2016. Unmanned aerial vehicles for high-throughput phenotyping and agronomic research. Plos One 11.

Sidike, P., Krieger, E., Alom, M.Z., Asari, V.K., Taha, T., 2017. A fast single-image super-resolution via directional edge-guided regularized extreme learning regression. Signal Image Video Process., 1–8

Singh, A., Ganapathysubramanian, B., Singh, A.K., Sarkar, S., 2016. Machine learning for high-throughput stress phenotyping in plants. Trends Plant Sci. 21, 110–124.

Smola, A.J., Schölkopf, B., 2004. A tutorial on support vector regression. Stat. Comput. 14, 199–222.

Strecha, C., Küng, O., Fua, P., 2012. 2012. EuroCOW.

Su, B.F., Xue, J.R., Xie, C.Y., Fang, Y.L., Song, Y.Y., Fuentes, S., 2016. Digital surface model applied to unmanned aerial vehicle based photogrammetry to assess potential biotic or abiotic effects on grapevine canopies. Int. J. Agric. Biol. Eng. 9, 119–130.

Tattaris, M., Reynolds, M.P., Chapman, S.C., 2016. A direct comparison of remote sensing approaches for high-throughput phenotyping in plant breeding. Front Plant Sci 7.

Thenkabail, P.S., Smith, R.B., De Pauw, E., 2000. Hyperspectral vegetation indices and their relationships with agricultural crop characteristics. Remote Sens. Environ. 71, 158–182.

Thoele, H., Ehlert, D., 2010. Biomass related nitrogen fertilization with a crop sensor. Appl. Eng. Agric. 26, 769–775.

Tilly, N., Aasen, H., Bareth, G., 2015. Fusion of plant height and vegetation indices for the estimation of barley biomass. Remote Sens.-Basel 7, 17291–17296 (vol 7, pg 11449, 2015).

Torres-Sanchez, J., Pena, J.M., de Castro, A.I., Lopez-Granados, F., 2014. Multi-temporal mapping of the vegetation fraction in early-season wheat fields using images from UAV. Comput. Electron. Agric. 103, 104–113.

Tuia, D., Verrelst, J., Alonso, L., Pérez-Cruz, F., Camps-Valls, G., 2011. Multioutput support vector regression for remote sensing biophysical parameter estimation. IEEE Geosci. Remote Sci. 8, 804–808.

Turner, D., Lucieer, A., Watson, C., 2012. An automated technique for generating georectified mosaics from ultra-high resolution unmanned aerial vehicle (UAV) imagery, based on structure from motion (SfM) point clouds. Remote Sens.-Basel 4, 1392–1410.

Ullah, S., 2013. Thermal Plants: Characterizing Vegetation Parameters Using Mid to Thermal Infrared Hyperspectral Remote Sensing. Universiteit Twente.

U.S. Geological Survey, 2016. USGS National Elevation Dataset (NED) 1 arc-second Downloadable Data Collection from The National Map 3D Elevation Program (3DEP) - National Geospatial Data Asset (NGDA) National Elevation Data Set (NED): U.S. Geological Survey.

Uto, K., Seki, H., Saito, G., Kosugi, Y., 2013. Characterization of rice paddies by a UAV-mounted miniature hyperspectral sensor system. IEEE J.-Stars 6, 851–860.

Verrelst, J., Alonso, L., Camps-Valls, G., Delegido, J., Moreno, J., 2012a. Retrieval of vegetation biophysical parameters using Gaussian process techniques. IEEE Trans. Geosci. Remote 50, 1832–1843.

Verrelst, J., Muñoz, J., Alonso, L., Delegido, J., Rivera, J.P., Camps-Valls, G., Moreno, J., 2012b. Machine learning regression algorithms for biophysical parameter retrieval: opportunities for Sentinel-2 and-3. Remote Sens. Environ. 118, 127–139.

Virlet, N., Lebourgeois, V., Martinez, S., Costes, E., Labbe, S., Regnard, J.L., 2014. Stress indicators based on airborne thermal imagery for field phenotyping a heterogeneous tree population for response to water constraints. J. Exp. Bot. 65, 5429–5442.

Wallace, L., 2013. Assessing the stability of canopy maps produced from UAV-LiDAR data. In: 2013 IEEE International on Geoscience and Remote Sensing Symposium (IGARSS). IEEE, pp. 3879–3882.

Walthall, C., Dulaney, W., Anderson, M., Norman, J., Fang, H., Liang, S., 2004. A comparison of empirical and neural network approaches for estimating corn and soybean leaf area index from Landsat ETM+ imagery. Remote Sens. Environ. 92, 465–474.

Wang, C., Nie, S., Xi, X., Luo, S., Sun, X., 2016. Estimating the biomass of maize with hyperspectral and LiDAR data. Remote Sens.-Basel 9, 11.

Wang, D.L., Xin, X.P., Shao, Q.Q., Brolly, M., Zhu, Z.L., Chen, J., 2017a. Modeling aboveground biomass in Hulunber grassland ecosystem by using unmanned aerial vehicle discrete lidar. Sensors-Basel 17.

Wang, D.P., Huang, J.L., Nie, L.X., Wang, F., Ling, X.X., Cui, K.H., Li, Y., Peng, S.B., 2017b. Integrated crop management practices for maximizing grain yield of double-season rice crop. Sci Rep-Uk 7.

Williams, D., Hinton, G., 1986. Learning representations by back-propagating errors. Nature 323, 533–538.

Yi, Q.X., Jiapaer, G., Chen, J.M., Bao, A.M., Wang, F.M., 2014. Different units of measurement of carotenoids estimation in cotton using hyperspectral indices and partial least square regression. ISPRS J. Photogramm. 91, 72–84.

Zaman-Allah, M., Vergara, O., Araus, J., Tarekegne, A., Magorokosho, C., Zarco-Tejada, P., Hornero, A., Albà, A.H., Das, B., Craufurd, P., 2015. Unmanned aerial platform-based multi-spectral imaging for field phenotyping of maize. Plant Methods 11, 35.

Zarco-Tejada, P.J., Diaz-Varela, R., Angileri, V., Loudjani, P., 2014. Tree height quantification using very high resolution imagery acquired from an unmanned aerial vehicle (UAV) and automatic 3D photo-reconstruction methods. Eur. J. Agron. 55, 89–99.

Zarco-Tejada, P.J., Gonzalez-Dugo, V., Berni, J.A.J., 2012. Fluorescence, temperature and narrow-band indices acquired from a UAV platform for water stress

detection using a micro-hyperspectral imager and a thermal camera. Remote Sens. Environ. 117, 322–337.
Zarco-Tejada, P.J., Guillen-Climent, M.L., Hernandez-Clemente, R., Catalina, A., Gonzalez, M.R., Martin, P., 2013. Estimating leaf carotenoid content in vineyards using high resolution hyperspectral imagery acquired from an unmanned aerial vehicle (UAV). Agric. For. Meteorol. 171, 281–294.
Zhang, C., Kovacs, J.M., 2012. The application of small unmanned aerial systems for precision agriculture: a review. Precision Agric. 13, 693–712.
Zhang, L., Zhang, D., Tian, F., 2016. SVM and ELM: Who Wins? Object Recognition with Deep Convolutional Features from ImageNet. In: Proceedings of ELM-2015, vol. 1. Springer, pp. 249–263.